Bootstrap resampling as a tool for radio-interferometric imaging fidelity assessment

Athol Kemball

National Center for Supercomputing Applications, University of Illinois at Urbana-Champaign, 605 E. Springfield Avenue, Champaign, IL 61820

and

Adam Martinsek

Department of Statistics, University of Illinois at Urbana-Champaign, 725 S. Wright Street, Champaign, IL 61820

ABSTRACT

We report on a numerical evaluation of the statistical bootstrap as a technique for radio-interferometric imaging fidelity assessment. The development of a fidelity assessment technique is an important scientific prerequisite for automated pipeline reduction of data from modern radio interferometers. We evaluate the statistical performance of two bootstrap methods, the model-based bootstrap and subsample bootstrap, against a Monte Carlo parametric simulation, using interferometric polarization calibration and imaging as the representative problem under study. We find both statistical resampling techniques to be viable approaches to radio-interferometric imaging fidelity assessment which merit further investigation. We also report on the development and implementation of a new self-calibration algorithm for radio-interferometric polarimetry which makes no approximations for the polarization source model.

Subject headings: techniques: image processing — methods: statistical — techniques: interferometric — techniques: polarimetric

1. Introduction

Radio interferometry produces astronomical images of unmatched spatial resolution and of unique scientific value. The images are formed by solving an inverse imaging problem connecting the spatial coherence of the incident radiation, gridded into the visibility plane orthogonal to the source direction, and the radio brightness distribution projected on the plane of the sky. An extensive review of this observing method is provided by Thompson, Moran, & Swenson (2001). The techniques used for indirect imaging in this discipline are well-established and robust, when used within the realm in which they are mathematically applicable. Best practices have been established in the community for their practical application based on algorithm research and evaluation, and common data reduction experience (Perley, Schwab, & Bridle 1989; Taylor, Carilli, & Perley 1999).

A central unsolved question, however, concerns the development of a quantitative method to assess the fidelity and precision of the reconstructed images at each pixel on the plane of the sky. Radio synthesis image formation requires a simultaneous solution for the source brightness distribution and instrumental calibration effects, including the effects of atmospheric propagation and the instrumental response of the antennas and receiving electronics of the system (Rogers et al. 1974). This joint solution is generally solved iteratively (Readhead & Wilkinson 1978), with an image deconvolution step per iteration to remove the effects of the sparse sampling of the measured correlation data in the visibility plane (Högbom 1974). Errors in calibration and imaging both introduce errors into the final reconstructed images. Formally, the inverse imaging problem admits an infinite family of solutions for the source brightness distribution due to the sparse sampling of the visibility data. However, the problem can be regularized by applying physically reasonable constraints, such as positivity and compact support, to provide a robust calibration and imaging method which is strongly convergent in practice (Thompson, Moran, & Swenson 2001).

An analytic solution for the fidelity of the reconstructed image is not tractable given the complex instrumental model and the common use of non-linear deconvolution methods. A method for quantitative fidelity assessment is, however, of vital scientific importance in radio interferometry. The increasing instrumental complexity and output data rates of current and future radio interferometers, such as the Atacama Large Millimeter Array (ALMA¹), the pre-cursor Combined Array for Research in Millimeter-wave Astronomy (CARMA²), the Expanded VLA Project (EVLA³), and the Square Kilometer Array (SKA⁴), require automated pipelined data reduction, as opposed to custom interactive reduction, if these telescopes are to achieve their full scientific potential and be accessible to the broadest astronomical user

¹http://www.alma.nrao.edu

²http://www.mmarray.org

³http://www.aoc.nrao.edu/evla

⁴http://www.skatelescope.org

community. This is particularly important for potential observers from other wavebands, or those who do not have a significant investment in specialized radio interferometric expertise at their local institutions. Pipelined data reduction can remove these barriers to entry, but requires a method for quantitative fidelity assessment to allow the statistical significance of features in the final science images to be clearly delineated. This is also true for general scientific analysis and interpretation of archived radio data, in repositories such as the National Virtual Observatory (NVO⁵). Apart from their importance in pipeline and archive analysis, we also note that fidelity assessment methods are useful in standard interactive data reduction, particularly for long-duration targeted imaging observations where high-fidelity is a specific goal.

Recent advances in techniques in computational statistics and the availability of leading-edge community resources for high-performance computing (HPC), allow fundamentally new approaches to be taken to the problem of radio-interferometric imaging fidelity assessment. We report here on the investigation of one such modern statistical technique, namely bootstrap resampling of dependent data (Lahiri 2003), applied to the test case of polarimetric calibration and imaging of Very Long Baseline Interferometry (VLBI) data. This test problem has been chosen for study as it is broadly representative of the calibration and imaging problems in radio interferometry in general, and is also of intrinsic scientific and technical interest. It is not, however, the only imaging application in radio interferometry for which fidelity assessment is scientifically important. Other such problems include, for example, high-fidelity imaging of strong, extended sources in total intensity, and we reserve their study for future work. We note the use of the bootstrap to assess the functional precision of medical tomography images in a related inverse imaging problem domain (Maitra 1997).

The advent of the Very Long Baseline Array (VLBA⁶), which was engineered with a uniform instrumental polarization response and a higher overall sensitivity than previous US VLBI arrays (Kellermann & Thompson 1985), has significantly broadened the scope and range of science possible using VLBI polarimetry (Wardle & Roberts 1994). Polarization VLBI studies are frequently concerned with imaging weak polarized emission, as common target sources such as continuum extra-galactic radio source cores typically have a degree of integrated linear polarization not exceeding several percent of the total Stokes *I* brightness (Cawthorne et al. 1993). Image fidelity assessment methods are therefore particularly relevant to VLBI polarimetry (Roberts, Wardle, & Brown 1994). We note that although other

⁵http://www.us-vo.org

⁶The National Radio Astronomy Observatory is operated by Associated Universities, Inc., under cooperative agreement with the National Science Foundation

emission processes studied with VLBI, such as maser emission, may have a higher degree of either linear or circular polarization than continuum synchrotron sources (Kemball 2002), it remains equally important to be able to assess the significance of weak polarized emission in imaging studies of these objects as well.

In this paper we explore the use of the statistical technique of bootstrap resampling to estimate the pixel-based variance in the output images produced by the calibration and imaging of simulated polarization data from the VLBA. These variance images are intercompared with results obtained by direct Monte Carlo simulation, and confirm the validity of the bootstrap approach in this domain.

The paper is structured as follows: Section 2 describes the theory of polarization calibration and bootstrap resampling. The details of the methods used in this numerical study are presented in Section 3 and the numerical results in Section 4. The discussion and conclusions are presented in Section 5 and Section 6 respectively.

2. Theory

2.1. The imaging equation for VLBI polarimetry

Radio-interferometric polarimetry, which allows imaging of the radio brightness in all four Stokes parameters $\{I,Q,U,V\}$, is possible if a sufficient subset of antennas in the array is equipped with orthogonal polarization receptors (usually crossed-linear or oppositely-polarized circular) and the correlator forms all available polarization cross-products between the independent polarization channels at each antenna on each baseline. The calibration algebra for interferometric polarimetry was first derived by Morris, Radhakrishnan, & Seielstad (1964), with further work provided by Conway & Kronberg (1969) and Weiler (1973). The analysis for the specialization of continuum VLBI polarimetry has been developed systematically over the past twenty years (Cotton et al. 1984; Roberts et al. 1984; Roberts, Brown, & Wardle 1991; Cotton 1993; Roberts, Wardle, & Brown 1994; Leppanen, Zensus, & Diamond 1995; Kemball, Diamond, & Pauliny-Toth 1996). A corresponding signal path analysis for spectral line polarization VLBI, including a formulation of the calibration and propagation effects along the signal path from the top of the atmosphere through the antennas, feeds, receiving electronics and correlator, was provided by Kemball (1993) and Kemball, Diamond, & Cotton (1995).

A general mathematical framework for radio-interferometric polarimetry is described in a series of papers by Hamaker, Bregman, & Sault (1996), Sault, Hamaker, & Bregman (1996), Hamaker & Bregman (1996) and Hamaker (2000). This series of papers (hereinafter

HBS) parametrizes the signal path analysis at each antenna as the product of a series of (2×2) Jones matrices, by analogy with their use in transmission optics. This mathematical formulation represents no new physics over earlier analyzes of the signal path and the resultant polarimetric interferometer response. However the use of Jones matrices and the outer matrix product allows a concise formulation in which the calibration algebra can be expressed independent of the choice of a specific polarization receptor basis, be that linear or circular.

The outer matrix product for two Jones matrices A and B, denoted $A \otimes B$, is cited by HBS as:

$$A \otimes B = \begin{pmatrix} a_{00}b_{00} & a_{00}b_{01} & a_{01}b_{00} & a_{01}b_{01} \\ a_{00}b_{10} & a_{00}b_{11} & a_{01}b_{10} & a_{01}b_{11} \\ a_{10}b_{00} & a_{10}b_{01} & a_{11}b_{00} & a_{11}b_{01} \\ a_{10}b_{10} & a_{10}b_{11} & a_{11}b_{10} & a_{11}b_{11} \end{pmatrix}$$

$$(1)$$

Each quadrant of $A \otimes B$ is formed as the product of the corresponding element in A times the matrix B. The outer product of two $n \times n$ matrices has dimension $n^2 \times n^2$.

(Cornwell 1995a) generalized the HBS framework to include image-plane calibration effects, leading to an imaging equation of the general form:

$$V_{mn} = \prod_{\kappa} \left[G_m^{\kappa} \otimes G_n^{\kappa*} \right] \int_{\Omega} \prod_{\kappa} \left[T_m^{\kappa}(\vec{\rho}) \otimes T_n^{\kappa*}(\vec{\rho}) \right] e^{-2\pi j \vec{b}_{mn} \cdot (\vec{\rho} - \vec{\rho_s})} K S(\vec{\rho}) d\Omega \tag{2}$$

where \otimes denotes the outer matrix product, $j = \sqrt{-1}$, $S(\vec{\rho})$ is the radio brightness expressed as a Stokes four-vector toward the unit direction $\vec{\rho} \in \Omega$, and Ω is the region of astronomical interest on the sky centered on $\vec{\rho_s}$,

$$S(\vec{\rho}) = \begin{pmatrix} I \\ Q \\ U \\ V \end{pmatrix} (\vec{\rho}) \tag{3}$$

 V_{mn} is the measured visibility correlation between antennas m and n in a polarization receptor basis $(p,q) \in \{(X,Y),(R,L)\}$, for linearly- and circularly-polarized feeds respectively,

$$V_{mn} = \begin{pmatrix} V^{pp} \\ V^{pq} \\ V^{qp} \\ V^{qq} \end{pmatrix}_{mn} \tag{4}$$

 G_m^{κ} is an element in the sub-series product of Jones matrices which have no direction dependence, $G_m^{\kappa} \neq f(\vec{\rho})$, and thus describes visibility-plane signal path corrections at antenna m of type κ , where κ enumerates the sub-types of the calibration corrections in the signal path. Examples of visibility-plane calibration correction sub-types enumerated by κ include those arising from bandpass and electronic gain corrections. In the image plane, T_m^{κ} is an element in the product of Jones matrices with direction dependence, $T_m^{\kappa} = f(\vec{\rho})$, thus describing image-plane corrections at antenna m of type κ , and K is a fixed (4×4) conversion matrix which maps the Stokes four-vector $S(\vec{\rho})$ into polarization correlation pairs V^{pq} in the receptor polarization basis.

We omit decorrelation losses (HBS) and baseline-dependent digital signal processing corrections (Cornwell 1995a) in this expression, as they are not relevant to the work presented in this paper. The individual Jones matrix elements for each correction matrix are expressed in the adopted polarization receptor basis $(\vec{e_p}, \vec{e_q})$ and can also be parametrized arbitrarily on parameters ξ_k defining an individual instrumental model:

$$G = \begin{pmatrix} g_{00}(\xi_k) & g_{01}(\xi_k) \\ g_{10}(\xi_k) & g_{11}(\xi_k) \end{pmatrix} \begin{pmatrix} \vec{e_p} \\ \vec{e_q} \end{pmatrix}$$
 (5)

The sets of Jones matrices in the visibility-plane, $\{G_m\}$, and the image-plane, $\{T_m\}$, model the calibration corrections for the full signal path at each antenna. These individual calibration components are enumerated in further detail by Cornwell (1995a), Noordam (1995), and Noordam (1996). For the chosen case of VLBI polarimetry used here to evaluate the bootstrap resampling for radio-interferometric imaging fidelity assessment, we restrict the instrumental corrections to the Jones matrices for the parallactic angle correction, $P_m = G_m^P$, and the instrumental polarization response, $D_m = G_m^D$. These formally both depend on direction, $\vec{\rho}$, but for the narrow field of view typical in VLBI we consider these as direction-independent corrections at the center of the field, with $P_m, D_m \in \{G_m\}$. These are the on-axis values accordingly. For the VLBA antennas, which have altitude-azimuth (alt-az) mounts and circularly polarized receptors,

$$P_m = \begin{pmatrix} e^{-j\alpha_m(t)} & 0\\ 0 & e^{j\alpha_m(t)} \end{pmatrix} \tag{6}$$

where $\alpha_m(t)$ is the time-variable parallactic angle at antenna m, which is known analytically (TMS). The instrumental polarization response, also known as the D-terms or polarization leakage (Morris, Radhakrishnan, & Seielstad 1964; Conway & Kronberg 1969), take the Jones matrix form:

$$D_m = \begin{pmatrix} 1 & d_m^p \\ d_m^q & 1 \end{pmatrix} \tag{7}$$

where $d_m^{(p,q)}$ are the traditional complex components of the *D*-term at antenna *m* for polarization (p,q) (Noordam 1995).

2.2. Strategies for VLBI instrumental polarization calibration

By design of the presented work, the VLBI polarimetry data considered here require no calibration for electronic gain amplitude or phase. Equivalently stated, there is no diagonal Jones matrix in $\{G_m\}$, outside of P_m or D_m , which needs to be applied to correct the data. This is the usual condition for polarization VLBI data in current data reduction practice before the final incremental solution for the polarization leakage terms. The residual problem of solving for D_m requires knowledge of $S(\vec{\rho})$ or a joint solution for $S(\vec{\rho})$ and D_m simultaneously, as is evident from equation 2. In general, this problem is more difficult for polarization VLBI than connected-element interferometry, due to the higher spatial resolution and the relative absence of calibrator sources with a known polarization structure at milliarcsecond (mas) resolution. A number of approximations for the source model polarization structure have been developed in the past to sharply reduce the number of free parameters \varkappa_l describing the source polarization model, and thus allow a single fit for the source model unknowns \varkappa_l and the D_m simultaneously. For an alt-az array such as the VLBA, each antenna has a sufficiently different variation of parallactic angle with time to allow these parameters to be separated. Expressed equivalently, the basis functions $e^{j\alpha_m(t)}$ are non-degenerate over a sufficient range in parallactic angle variation. The source approximation methods in common VLBI use are summarized by Kemball (1999). These approximations include assumptions of: i) a linearly-unpolarized calibrator, (Q, U) = 0 (Roberts et al. 1984); ii) an unresolved calibrator, $(Q, U) = \varkappa$ (Cotton et al. 1984); iii) a similarity approximation, $Q + jU = \varkappa I$ (Cotton 1993); iv) a multi-component similarity approximation, $\sum_{l} (Q_l + jU_l) = \varkappa_l I_l$ (Leppanen, Zensus, & Diamond 1995), and, v) a spectral-line approximation, $Q(\nu) + jU(\nu) = \varkappa_{\nu}I(\nu)$ (Kemball and Diamond 1997). This family of solution methods will be referred to as source approximation methods in what follows. These approximations reduce the source polarization model parameters to fewer than required for a fully general polarization model by fixing the scaling factor \varkappa per image (iii), per Gaussian image component (iv), or per spectral channel (v) respectively.

It has also been common practice in polarization VLBI to linearize the feed leakage calibration equations by ignoring terms of order $O(D^2)$ or $O(D \cdot (Q + jU))$ (Roberts et al. 1984) and to use only the resulting linear equations for the cross-polarized visibilities (V^{pq}, V^{qp}) in a linear fit for \varkappa_i and D_m (Cotton 1993; Kemball, Diamond, & Cotton 1995; Leppanen, Zensus, & Diamond 1995; Kemball and Diamond 1997). This linearization has also typically been applied to the equation inverse when correcting the visibility data for the polarization leakage D-terms. The use of the matrix-based HBS framework implicitly includes all terms without linearization.

2.3. Polarization self-calibration

Polarization self-calibration has been proposed frequently in the literature as a likely optimal technique for solving simultaneously for the source model and the instrumental polarization response (Roberts, Wardle, & Brown 1994; Sault, Hamaker, & Bregman 1996). This is by direct analogy with the cornerstone role self-calibration plays in radio interferometry in allowing a simultaneous solution for the total intensity distribution and complex antenna-based electronic gains. A recent review of electronic gain self-calibration is provided by Cornwell & Fomalont (1999). Several of the source approximation methods described in the previous section have already been applied iteratively, as a variant of polarization self-calibration (Kemball, Diamond, & Pauliny-Toth 1996; Kemball and Diamond 1997).

A simple definition of polarization self-calibration is that of an joint (often iterative) solution for $S(\vec{\rho})$ and D_m within a calibration framework for radio-interferometric polarimetry, with optional constraints applied in the visibility and image planes to regularize the solution as required. As such, it is the direct analog of standard total intensity phase and amplitude self-calibration. In the HBS framework, general self-calibration is simply any joint solution for a set of unsolved Jones calibration matrices in $\{G_m\}$ and $\{T_m\}$ simultaneously with the source brightness distribution $S(\vec{\rho})$; all are free parameters in the imaging equation on a equal footing. In this nomenclature, polarization self-calibration, as defined above, is a simple subset of general self-calibration in the imaging equation formalism.

In the imaging equation framework [2], given an estimate for D_m and the known analytic P_m , the source brightness can be determined from $\frac{\partial \chi^2}{\partial S(\vec{\rho})}$ and the use of standard deconvolution techniques, as described by (Cornwell 1995b), where χ^2 is computed as the difference between the observed and predicted visibility data. Conversely, given an estimate of $S(\vec{\rho})$,

and the known analytic P_m , χ^2 can be formed at the position of the unknown D_m in the imaging equation by computing contributions from the right-hand and left-hand sides of [2] respectively through to the position of D_m in $\prod [G_m \otimes G_m^*]$ and forming χ^2 by inserting the current value of the D_m matrix at that position (Cornwell & Wieringa 1996). This also allows a direct computation of $\frac{\partial \chi^2}{\partial D_m}$, which can be used in a non-linear fit for the off-diagonal Jones matrix elements of D_m in each polarization solution interval. We re-express this mathematically by defining two operators, \mathcal{R}^{β} and \mathcal{L}^{β} , which operate from the right- and left-hand sides of the imaging equation respectively, through to the position of a visibility calibration component G_m^{β} being solved for. The operators yield 4-vectors containing the accumulated product of visibility cross-correlations at that index point in the imaging equation. For baseline mn,

$$\mathcal{L}_{mn}^{\beta} = V_{mn} \prod_{\kappa}^{\beta-1} [G_m^{\kappa} \otimes G_n^{*\kappa}]^{-1}$$

$$\mathcal{R}_{mn}^{\beta} = \prod_{\kappa=\beta+1} [G_m^{\kappa} \otimes G_n^{*\kappa}] \int_{\Omega} \prod_{\kappa} [T_m^{\kappa}(\vec{\rho}) \otimes T_n^{\kappa*}(\vec{\rho})] e^{-2\pi j \vec{b}_{mn} \cdot (\vec{\rho} - \vec{\rho}_{\vec{s}})} K S(\vec{\rho}) d\Omega \qquad (9)$$

$$\mathcal{R}_{mn}^{\beta} = \prod_{\kappa=\beta+1} \left[G_m^{\kappa} \otimes G_n^{*\kappa} \right] \int_{\Omega} \prod_{\kappa} \left[T_m^{\kappa}(\vec{\rho}) \otimes T_n^{\kappa*}(\vec{\rho}) \right] e^{-2\pi j \vec{b}_{mn} \cdot (\vec{\rho} - \vec{\rho}_s)} K S(\vec{\rho}) d\Omega \tag{9}$$

The calibration solver minimizes,

$$\chi^2 = \sum_{mn} \| (G_m^{\beta} \otimes G_n^{*\beta}) \mathcal{R}_{mn}^{\beta} - \mathcal{L}_{mn}^{\beta} \|$$
 (10)

Polarization self-calibration can be achieved in this framework using an iterative solver which starts with an initial value, D_m^0 , for each D Jones matrix, and iterates with optional visibility- or image-plane constraints to solve successively for $S(\vec{\rho})$ and the set of D_m per antenna and polarization solution interval, within the imaging equation model. The data are pre-averaged in the fit over time intervals short with respect to the maxima $\left|\frac{d\alpha_m(t)}{dt}\right|$ and $\left|\frac{dS(\vec{\rho})}{dt}\right|$ where t is used here as a parameter along the uv-tracks in the visibility plane. We note that χ^2 is formed here from the visibility 4-vectors, including cross-polarized correlations. The imaging deconvolution similarly uses the 4-vector of full polarization intensities.

2.4. Imaging fidelity assessment

The visibility data measured at loci in the uv-plane for each projected baseline mnconstitute a time-series of complex observed data, denoted here as: $\{V_{mn}^{obs}(u_k, v_k, t_k), k = 1\}$ $1, N_{mn}, \forall (m, n)$. We adopt a simple additive noise model for the measured visibility data:

$$V_{mn}^{obs} = V_{mn} + \mathcal{N} \tag{11}$$

where V_{mn} is given by equation [2], and \mathcal{N} is a random phasor drawn from the complex normal probability density for $\mathcal{CN}(0, \sigma_{th}^2)$ of zero mean and variance σ_{th}^2 . We adopt the statistical nomenclature here of Kay (1993) for complex random variables. The noise contribution is independent and identically distributed (IID). For a radio interferometer comprised of uniform array elements of system equivalent flux density SEFD (a fundamental parameter of antenna sensitivity), bandwidth $\Delta \nu$, and a sample integration time Δt , the thermal noise variance is given in the form (TMS):

$$\sigma_{th}^2 = \frac{SEFD^2}{2\triangle\nu\triangle t} \tag{12}$$

The complete set of measured visibility data $\{V_{mn}^{obs}(u_k, v_k, t_k), k = 1, N_{mn}, \forall (m, n)\}$ can be regarded as a single statistical realization of a sequence of random variables $\{V_1, V_2, ..., V_N\}$ of sample size N from a joint multivariate probability density function (PDF),

$$p(\mathcal{V}; S(\vec{\rho}), G_m^{\kappa}, T_m^{\kappa}) = \frac{1}{\pi^N \sigma_{th}^{2N}} e^{-[(\mathcal{V} - V_{mn})^H C_{\mathcal{V}}^{-1} (\mathcal{V} - V_{mn})]}$$
(13)

where the covariance matrix $C_{\mathcal{V}} = \sigma_{th}^2 U$, superscript H denotes conjugate transpose (Kay 1993), U is an $(N \times N)$ unit diagonal matrix, and the imaging equation [2] yields $V_{mn} = f(S(\vec{\rho}), G_m^{\kappa}, T_m^{\kappa})$. Although this is a parametric distribution, here in terms of $(S(\vec{\rho}), G_m^{\kappa}, T_m^{\kappa})$, these quantities are not known at the time of observation, and are determined by the calibration and imaging process used in data reduction. We consider any solvers for the calibration matrices $(G_m^{\kappa}, T_m^{\kappa})$ or the source brightness distribution $S(\vec{\rho})$ as statistical point estimators for these parameters and denote these estimators as $\hat{S}(\vec{\rho}), \hat{G}_m^{\kappa}$, and \hat{T}_m^{κ} . This perspective connects the observed visibility data $\{V_{mn}^{obs}(u_k, v_k, t_k), k = 1, N_{mn}, \forall (m, n)\}$ and the unknown source brightness distribution and calibration parameters appearing in the PDF, in the form of a standard statistical inference problem. In this context, the problem of imaging fidelity assessment is equivalent to that of determining the sampling distribution properties of the estimators $\hat{S}(\vec{\rho}), \hat{G}_m^{\kappa}$, and \hat{T}_m^{κ} . The imaging problem is assumed regularized, and therefore convergent and robust, in this analysis, in order to remove the poor conditioning implicit in the sparse sampling in the uv-plane. We omit the explicit choice of basis representation for $S(\vec{\rho})$; this could be pixel-based or of functional form.

We denote the sampling distribution of $\hat{S}(\vec{\rho})$ as $\mathcal{F}_{\hat{S}(\vec{\rho})}$. As the parent distribution $p(\mathcal{V}; S(\vec{\rho}), G_m^{\kappa}, T_m^{\kappa})$ for the observed visibility data is unknown, the sampling distribution

 $\mathcal{F}_{\hat{S}(\vec{\rho})}$ is also unknown a priori. We are physically and logistically constrained from measuring $p(\mathcal{V}; S(\vec{\rho}), G_m^{\kappa}, T_m^{\kappa})$ by drawing all potential realizations of the visibility time series from the parent population; each observing run is unique in terms of the instrumental and atmospheric conditions, quite apart from the logistical impracticality of this approach. In addition, if the calibration corrections are imperfectly modeled in any significant sense, $G_m^{\kappa} = f(\xi_l)$, the parent PDF will differ in mathematical form from the assumed model $p(\mathcal{V}; S(\vec{\rho}), G_m^{\kappa}, T_m^{\kappa})$. Errors in the form of the parametric model compromise the statistical inference based on that model.

2.5. Bootstrap resampling

Bootstrap resampling techniques offer an alternative statistical inference method which is not as sensitive to errors in the assumed model and does not require that the problem be analytically tractable. This method constructs statistical resamples from the measured data realization which mirror the statistical properties of the unknown parent population. Developed by Efron (1979) for IID data, this method has proved to be a powerful technique in modern computational statistics, with increasingly broad applicability. It has undergone significant theoretical development since its inception and modern reviews are provided by Shao & Tu (1995), Davison & Hinkley (1997), Chernick (1999), and Lahiri (2003). Bootstrap techniques have also been extended to the case of statistically dependent data which are not IID. This question is considered in detail in a monograph by Lahiri (2003), and is of particular importance for our study. The observed visibility data in radio interferometry are generated by a process with long-range statistical dependence, defined to first order by the Fourier transform of the source brightness distribution to the visibility uv-plane [2]. Other bootstrap resampling techniques, such as the jackknife and general subsampling methods (Shao & Tu 1995; Politis, Romano, & Wolf 1999), are also relevant to resampling of dependent data (Lahiri 2003).

A single measured realization $\{V_{mn}^{obs}(u_k, v_k, t_k), k = 1, N_{mn}, \forall (m, n)\}$ of the random process can be used to construct a distribution function $\tilde{p}(\mathcal{V}; S(\vec{\rho}), G_m^{\kappa}, T_m^{\kappa})$ from which statistical resamples \mathcal{V}^* can be drawn. The bootstrap principle requires that the statistical relationship between \mathcal{V}^* and $\tilde{p}(\mathcal{V}; S(\vec{\rho}), G_m^{\kappa}, T_m^{\kappa})$ mirror that between \mathcal{V} and $p(\mathcal{V}; S(\vec{\rho}), G_m^{\kappa}, T_m^{\kappa})$ (Lahiri 2003). We consider the specific choice for $\tilde{p}(\mathcal{V}; S(\vec{\rho}), G_m^{\kappa}, T_m^{\kappa})$ in further detail below.

We denote resamples drawn from $\tilde{p}(\mathcal{V}; S(\vec{\rho}), G_m^{\kappa}, T_m^{\kappa})$ conditional on the observed data $\{V_{mn}^{obs}(u_k, v_k, t_k), k = 1, N_{mn}, \forall (m, n)\}$ as $\{V_{mn}^{obs}(u_k, v_k, t_k), k = 1, N_{mn}, \forall (m, n)\}_{1..N_s}^*$; when acted on by the imaging estimator $\hat{S}(\vec{\rho})$, they yield S_N^* . The bootstrap estimate of the sampling distribution, $\hat{\mathcal{F}}_{\hat{S}(\vec{\rho})}$ can then be obtained from the distribution of S_N^* .

The primary statistical requirement on successful use of the bootstrap method is that the relationship between the resamples and the PDF derived from the data realization accurately reflect the corresponding relationship between the parent population and the observed data. For IID data, the empirical probability distribution function is an optimal choice: $\tilde{p}(\bullet) = N^{-1} \sum_{k=1}^{N} \|(\mathcal{V} \leq \bullet)$, where the indicator function $\|(A) = 1$ if A is true, else zero (Lahiri 2003). For IID data, resamples can be drawn from the empirical distribution function directly, with replacement, to generate a valid bootstrap ensemble (Davison & Hinkley 1997).

The IID bootstrap is not statistically valid, however, for the case of dependent data Singh (1981), and modifications to address dependence are reviewed by (Lahiri 2003). We summarize them here in several broad categories: (i) block bootstraps; (ii) model-based bootstraps, and; (iii) subsampling bootstraps. Block bootstrap methods resample the data in blocks of sufficient length to capture the bulk of the auto-covariance dependence information in the data. Model-based bootstrap methods model and remove the statistical dependence from the data and apply the direct bootstrap to the residuals, assumed then to be IID (Lahiri 2003). In this bootstrap method, the model fit is tailored to the process generating the data. Subsampling draws unmodified fractional resamples from the data; as such it is a generalization of the delete-d jackknife (Politis, Romano, & Wolf 1999). Subsampling preserves directly the long-range statistical dependence in the resamples.

Although the bootstrap is a computationally intensive technique, geometric advances in available HPC resources make this technique readily applicable as an approach to radio interferometry imaging fidelity assessment. We discuss the practical evaluation of this technique with radio interferometry data in subsequent sections.

3. Simulation methods

We have conducted several numerical studies to inter-compare the results of bootstrap resampling with those obtained by direct Monte Carlo simulation, as a means to evaluate the applicability and usefulness of bootstrap resampling techniques in radio interferometric imaging fidelity assessment. As noted in the introduction, we have chosen VLBI polarization self-calibration and imaging as the test case for evaluation, both as it is broadly representative of general calibration and imaging in radio interferometry, and also because of its intrinsic scientific and technical interest. In the language and formulation of Section 2.4, we seek to measure the sampling distribution properties of the imaging estimator using several candidate bootstrap resampling techniques, in order to assess their statistical performance in this problem domain.

3.1. Polarization self-calibration heuristic

For the numerical studies conducted here, we have developed a polarization self-calibration algorithm based on the general principles outlined in Section 2.3. We do not consider the detailed scientific optimization of the polarization self-calibration algorithm here, as this aspect is not central to our study of the bootstrap method. We require only that the algorithm be broadly representative of typical calibration and imaging data reduction processes in radio interferometry.

We adopt a simple polarization self-calibration heuristic accordingly, starting with an initial unit diagonal D Jones matrix at each antenna,

$$D_m^0 = \begin{pmatrix} 1 & 0 \\ 0 & 1 \end{pmatrix} \tag{14}$$

and iterating without any visibility- or image-plane constraints to solve successively for $S(\vec{\rho})$ and each D_m per antenna, varying only the off-diagonal D Jones terms. The data were pre-averaged to 5 seconds by the solver, and the D Jones solutions were assumed to have no time-dependence. CLEAN deconvolution was used during imaging, with a stopping threshold equal to the expected thermal noise limit; this deconvolution threshold was held constant for all self-calibration cycles. In this implementation, ten iterations of calibration and imaging were performed using non-progressive self-calibration, in which the uncorrected observed data were used in each cycle, as opposed to the corrected data from the previous cycle.

Iterative polarization self-calibration has not been used extensively in VLBI polarimetry partly due to the lack of software support in existing data reduction packages. The basic AIPS++⁷ package implements the imaging equation [2] and the HBS framework. For the applications developed here, we modified a reference version of the AIPS++ code base⁸, held constant for reproducibility across the course of this work, and used the calibration solver and imaging implementation available in the package at that time. Additional utilities for bootstrap resampling and analysis were also developed. These capabilites are intended for future public release in a local package.

⁷http://aips2.nrao.edu

 $^{^{8}}v1.8 \# 667 \text{ from } 2003$

3.2. Fidelity simulations

3.2.1. Simulation configuration

For these studies we chose to simulate single-channel data from the VLBA, at an observing frequency of 43.0 GHz. Data for a source at $(\alpha_{2000} = 12^h, \delta_{2000} = +80^{\text{deg}})$ were generated for all ten VLBA antennas in a set of 15 min scans starting at $\{t_k = (k-1)^h \text{ UT}, k = 1, 20\},\$ on an adopted date of 1 Feb 2003, using a correlator integration time $\Delta t = 2$ sec. The visibility data were generated in full polarization in a circular basis $\{RR, LR, RL, LL\}$, incorporating arbitrarily chosen instrumental D-terms, which are tabulated for each antenna in table 1. The D-terms were chosen randomly but have a similar mean order of magnitude as those expected for the VLBA as a whole at this frequency. The source brightness distribution was chosen randomly as a pair of unit flux density elliptical Gaussian components matched to the resolution of the array, with properties summarized in table 2, and plotted in Stokes $\{I, Q, U, V\}$ in figure 1. Their integrated polarization intensities in each polarization were also chosen at random, but are of the same order as might be observed for 43 GHz SiO maser components using the VLBA. The parallactic angle of the Pie Town (PT) antenna at the center of the array varied from -21° , through -176° near transit, to $+33^{\circ}$ at the end of the simulation. This is plotted in figure 2. The array resolution for this synthesis was ~ 150 μas in uniform weighting. Additive thermal noise was computed for each integration interval [11], using a nominal SEFD of 1436 Jy published for the VLBA 7mm band⁹. The data were generated at an image signal-to-noise ratio (SNR) of approximately 1300:1, as defined by the ratio of the peak source brightness to the off-source root-mean-square (rms) noise. This sensitivity is equivalent to that obtained by observing the unit flux density source components in an 8 MHz bandwidth, or the same source components increased in flux density by a factor of 16, in a typical SiO channel bandwidth of $\frac{1}{32}$ MHz. We adopted a normalized flux density scale for the source model in this work to allow different numerical results to be inter-compared readily, and a direct calculation of the dynamic range as the inverse rms.

3.2.2. Monte Carlo simulation

As the first step in the evaluation of bootstrap resampling, a reference statistical sample containing $N_s = 256$ realizations was generated by Monte Carlo simulation using the parametric model [13] and the array simulation configuration described above. The resulting Monte Carlo sample consisted of 256 simulated observed visibility time series data

⁹http://www.aoc.nrao.edu/vlba/obstatus/obssum/obssum.html

 $\{V_{mn}^{obs}(u_k,v_k,t_k),\ k=1,N_{mn},\ \forall\ (m,n)\}_{1..N_s}^{MC}$. The data were generated using a modified version of the task DTSIM, originally developed by the author in the AIPS¹⁰ package, so that the data would be generated and reduced in separate packages. Each realization was reduced using the polarization self-calibration and imaging heuristic described above, which is equivalent to the application of the imaging estimator $\hat{S}(\vec{\rho})$ defined in Section 2.4. We chose $S(\vec{\rho})$ to represent the final restored image in a pixel basis S_{xy} , and computed estimator statistics for $\hat{S}(\vec{\rho})$ in this basis over the set of N_s restored images obtained from application of the imaging estimator to the full Monte Carlo sample. A fixed circular restoring beam of full-width half-maximum (FWHM) equal to 156.007 μas was used for all images, set to the geometric mean of the beam in uniform weighting for the uv-coverage of the simulated data, which is shown in figure 3. All images were formed of size (256×256) pixels with a pixel spacing of 30 μas .

The imaging estimator bias and mean-squared error (MSE) were computed per pixel with respect to the known source brightness model convolved with the fixed restoring beam, as shown in figure 1. The mean and variance of the sampling distribution $\mathcal{F}_{\hat{S}(\vec{\rho})}$ of the estimator $\hat{S}(\vec{\rho})$, were similarly computed per pixel over the sample of N_s restored images. The variance was computed using the approximation $N_s^{-1} \sum (S_{xy}^2) - \bar{S}_{xy}^2$, for computational efficiency. The MSE per pixel was computed as $N_s^{-1} \sum (S_{xy} - \check{S}_{xy})^2$, where \check{S}_{xy} is the known true source brightness model convolved with the fixed restoring beam. Each statistic was computed per Stokes polarization $\{I, Q, U, V\}$ and per polarization self-calibration iteration number, across all N_s realizations. Similar estimator statistics were also accumulated per antenna and self-calibration iteration number for the polarization calibration estimators \hat{G}_m^D for each D Jones matrix determined by the polarization self-calibration and imaging solvers.

The estimator sampling distribution properties estimated using Monte Carlo simulation were used as the reference in assessing the statistical performance of the bootstrap techniques. In practical radio interferometry, direct Monte Carlo simulation of this form is not practical, as there is no a priori knowledge of the exact source brightness distribution and calibration matrix values.

3.2.3. Bootstrap simulations

We randomly chose the 127th realization $\{V_{mn}^{obs}(u_k, v_k, t_k), k = 1, N_{mn}, \forall (m, n)\}_{127}^{MC}$ from the Monte Carlo sample as input to the bootstrap resampling numerical studies. We

¹⁰http://www.aoc.nrao.edu/aips

resampled from this template realization using both model-based bootstrap methods and subsampling techniques, and generated in each case a sample of size $N_s = 256$ resampled observed visibility time series $\{V_{mn}^{obs}(u_k, v_k, t_k), k = 1, N_{mn}, \forall (m, n)\}_{1..N_s}^*$. The block bootstrap was not evaluated in this study due to the known long-range dependence in the data. The polarization self-calibration imaging estimator $\hat{S}(\bar{\rho})$ was applied to each realization and pixel-based estimator statistics computed across the S_{xy}^* in the same manner as were computed for the Monte Carlo sample described above. These statistics estimate the bootstrap sampling distribution $\hat{\mathcal{F}}_{\hat{S}(\bar{\rho})}$ and can be inter-compared with those obtained from the Monte Carlo sample to evaluate the statistical performance of the bootstrap.

For the model-based bootstrap, we adopted a piece-wise polynomial model for the real and imaginary parts of the observed visibility time series as a model of the long-term dependence in the data. A model of the form:

$$V_{mn}^{obs}(u_k, v_k, t_k) = \left(\sum_{l=0}^{N_p} a_l t_k^l + j \sum_{l=0}^{N_p} b_l t_k^l\right)$$
 (15)

was fit over successive bootstrap model intervals $\triangle t_b$ on each baseline, using least-squares minimization and a conjugate-gradient solver as implemented in the OptSolve++ package¹¹. The lowest polynomial degree was used in each solution interval which yielded convergence. The model residuals,

$$V_{mn}^{resid}(u_k, v_k, t_k) = V_{mn}^{obs}(u_k, v_k, t_k) - \left(\sum_{l=0}^{N_p} a_l t_k^l + j \sum_{l=0}^{N_p} b_l t_k^l\right)$$
(16)

were re-centered to avoid introducing bias (Lahiri 2003; Davison & Hinkley 1997),

$$V_{mn}^{resid'}(u_k, v_k, t_k) = V_{mn}^{resid}(u_k, v_k, t_k) - N_{\triangle t_b}^{-1} \sum_{\triangle t_b} V_{mn}^{resid}(u_k, v_k, t_k)$$
 (17)

and resampled, uniformly and randomly, with replacement, to yield $V_{mn}^{resid''}(u_k, v_k, t_k)$. The bootstrap resample for each $\triangle t_b$ was then constituted as:

$$V_{mn}^{*}(u_k, v_k, t_k) = \left(\sum_{l=0}^{N_p} a_l t_k^l + j \sum_{l=0}^{N_p} b_l t_k^l\right) + V_{mn}^{resid''}(u_k, v_k, t_k)$$
(18)

¹¹OptSolve++ is distributed by Tech-X corporation (http://www.techxhome.com)

Four model-based bootstrap runs were performed, which are labeled M1 through M4. The bootstrap parameters used for each run are summarized in table 3.

For the subsampling method, visibility points were deleted from the template realization randomly, avoiding repeated points, until a specified fraction, f_s , of the total number of visibility points in each sample were removed for each subsample realization generated. Each subsample realization was processed using the imaging estimator $\hat{S}(\vec{\rho})$ as used previously, and the same estimator statistics accumulated over the sample of restored images as were computed for the model-based bootstrap and Monte Carlo runs. Four subsample bootstrap runs were performed, labeled S1 through S4. The parameters used for each subsample run are summarized in table 4.

3.2.4. HPC implementation

All of the preceding Monte Carlo, bootstrap and subsample imaging estimator runs were computed on the public HPC Linux clusters deployed as a community resource by NCSA. Many of the bootstrap sample generation runs were also run in an HPC environment, but some were executed on a single workstation where possible. The parallel imaging estimator runs were mapped across the cluster nodes by assigning subsets of realizations to client nodes, and combining the partial statistical accumulations from each client node serially on a single node at the end of the run. A large degree of parallelism was achieved in these runs due to the limited communication needs between client nodes in this application. We typically ran over 32-64 cluster nodes, in individual runs of 4-8 hours duration. The duration depended on the underlying single-CPU performance of the specified cluster used. We expect these runs to scale efficiently to larger number of cluster nodes as they are well-matched to a loosely-coupled HPC architecture of this type.

4. Simulation results

4.1. Monte Carlo simulations

For the Monte Carlo simulations discussed in the previous section, we plot the total MSE for the calibration estimator \hat{G}_{m}^{D} , summed over all antennas m, against polarization self-calibration iteration number in figure 4.

The MSE, bias, and variance of the pixel-based imaging estimator $\hat{S}(\vec{\rho})$ are plotted for the restored Stokes $\{Q,U\}$ images, at self-calibration iteration numbers 1 and 10, in figure 5

and figure 6 respectively.

4.2. Bootstrap simulations

To assess the statistical performance of the model-based and subsampling bootstrap methods, we have computed a goodness-of-fit statistic which compares the variance image, var_{xy} , obtained by the imaging estimator for a particular bootstrap method against the corresponding reference variance image derived from Monte Carlo simulation, var_{xy}^{MC} . For the subsample bootstrap, the estimator statistics need to be scaled by a factor expected to be proportional to $\sim N(1-f_s)^a$ (Davison & Hinkley 1997), as derived for the delete-d jackknife, where the exponent, a, is dependent on the details of the individual model. We estimated the mean scaling factor, v_f , by summing over the inner quarter and over all Stokes polarizations $\{I, Q, U, V\}$ of the ratio image,

$$v_f = \frac{1}{N} \sum_{IQUV} \sum_{\Omega_{\frac{1}{A}}} \left(\frac{var_{xy}}{var_{xy}^{MC}} \right)$$
 (19)

A goodness-of-fit statistic, v_{MSE} , was then computed over the same image region and polarization set, as:

$$v_{MSE} = \frac{1}{N} \sum_{IQUV} \sum_{\Omega_{\frac{1}{4}}} \left(\frac{var_{xy}}{v_f} - var_{xy}^{MC} \right)^2$$
 (20)

These values are summarized for the model-based and subsample bootstrap runs in table 5. For reference, the bootstrap parameters for the model-based and subsample bootstrap runs are summarized in table 3 and table 4 respectively.

The variance images in Stokes $\{Q, U\}$ for the final polarization self-calibration iteration, obtained from the bootstrap runs, are plotted in figure 7, figure 8, figure 9, and figure 10.

The variation of scaling factor, v_f , with subsample delete fraction, f_s , is plotted in figure 11.

5. Discussion

The polarization self-calibration algorithm developed as part of this study of the bootstrap method, has a convergence rate for these data, shown in figure 4, that is steeper than exponential as a function of iteration number. The scope of the current study does not allow us to extrapolate the quantitative statistical properties of this calibration estimator to all potential practical applications, but we believe this to be a viable, general technique for solving for instrumental polarization in radio interferometry. Most importantly, it requires no polarization source model approximation, with the attendant systematic errors which may arise in this case. As is common for all polarization calibration algorithms in this class, we expect the solver to be sensitive to the degree of mutual degeneracy of the parallactic angle basis functions at each antenna (Conway & Kronberg 1969; Leppanen, Zensus, & Diamond 1995; Sault, Hamaker, & Bregman 1996), which can invariably be equivalently quantified in terms of the maximum range in parallactic angle coverage for the array as a whole. As noted earlier, the simulated data used in this study were chosen to have good coverage in parallactic angle.

Intuitively, we expect rapid convergence for polarization self-calibration algorithms from considering simple information arguments. For an interferometric observation of $N_{\triangle t}$ self-calibration intervals, using an array of N_{ant} elements, the number of self-calibration unknowns is $N_{\triangle t}N_{ant}$, and the number of knowns, defined by the data, is $\frac{N_tN_{ant}(N_{ant}-1)}{2}$, where N_t is the number of unique time-stamps in the observed visibility data. The ratio of knowns to unknowns is therefore $r = \frac{N_t(N_{ant}-1)}{2N_{\triangle t}}$. For conventional amplitude and phase self-calibration, $N_t \sim N_{\triangle t}$, and $r \sim \frac{N_{ant}}{2}$. For polarization self-calibration, the D-terms have slowly-varying time-dependence, $N_{\triangle t} \sim 1$, and $r \sim \frac{N_tN_{ant}}{2}$. This ratio is significantly higher than for amplitude and phase self-calibration and we expect a steeper rate of convergence as a result. As a corollary, given that the number of free parameters being solved for in polarization self-calibration is small relative to the number of visibility data points, it is more difficult to absorb coherent source brightness distribution errors in the calibration corrections than in conventional amplitude and phase self-calibration. This is dependent on the range of parallactic angle coverage however.

This paper has considered the common case of constant, visibility-plane polarization calibration, but this polarization self-calibration algorithm can, in principle, be used to solve for time- and direction-dependent instrumental polarization corrections. This is required for high-fidelity, wide-field imaging studies but is not a routine mode of radio interferometer calibration at present. This is a subject for future study but we anticipate that the algorithm performance in this case will depend on the accuracy and number of free parameters in the parametrization adopted for the time- and direction-dependence of the D Jones polarization

corrections.

Further information on the properties of the polarization self-calibration algorithm can be obtained by examining the imaging estimator statistics for the Monte Carlo sample, plotted in figure 5 and figure 6. At the first iteration, D Jones matrix errors dominate, and the magnitude of the estimator bias is higher across the image as a result. At this iteration, the imaging estimator MSE is dominated by the estimator bias. At the final self-calibration iteration the D Jones matrix corrections are better constrained, and the bias is accordingly reduced. At this point the imaging estimator MSE is dominated by the estimator variance. Both calibration and deconvolution errors contribute to the measured imaging estimator statistics. To first order, errors in the estimated D Jones calibration corrections corrupt the cross-polarized visibility data with proportional fractions of the Stokes I visibility (Roberts, Wardle, & Brown 1994), so the variance in Stokes Q and U does not scale linearly with the underlying Stokes Q or U intensity at each pixel.

The statistical performance of the model-based bootstrap, over runs M1 to M4, can be assessed by examining the goodness-of-fit statistic, v_{MSE} , tabulated in table 5, as well as the imaging estimator statistics plotted in figure 7 and figure 8. We expect optimal performance for the model-based bootstrap when the bootstrap model interval, $\triangle t_b$, is sufficiently long for adequate SNR in the fit to the bootstrap model parameters, but not so long as to invalidate the functional model for the statistical dependence in the data. The goodness-of-fit statistics listed in table 5, which capture the degree to which the bootstrap imaging variance matches that obtained from the reference Monte Carlo sample, suggest that run M3 reflects the optimal choice of model-based bootstrap run parameters for the data used in this study. Run M3 has the lowest v_{MSE} ; therefore its variance estimates have the best overall fit to the image variance obtained by direct Monte Carlo simulation.

It is clear, however, both from the tabulated goodness-of-fit statistic v_{MSE} , and the imaging estimator statistics, that the model-based bootstrap performs well over a fairly broad range of Δt_b and N_p ; the values of these parameters used for the runs M1 to M4 are tabulated in table 3. We find this technique to be relatively robust with respect to the detailed bootstrap model assumptions, and therefore easy to use in practice. This robustness over a wide range of tuning parameters is a significant advantage of the model-based bootstrap. There are, however, differences between the model-based bootstrap resamples, M1 to M4. As this is a numerical simulation study, we know the parent population distribution [13], and can compare the empirical distribution of the resampled data against the known parent distribution. The closer the match the better the performance of the underlying bootstrap method. We plot this in the form of a cumulative distribution function (CDF) comparison in figure 12, for the real and imaginary parts of the data separately, for a randomly chosen

visibility row number 1000, in polarization cross-correlation LR. The empirical CDF for the reference Monte Carlo sample is plotted in figure 13. We denote the empirical CDF for the resampled data as $\tilde{c}^{(R,I)}(\mathcal{V})$, and the true parent CDF as $c^{(R,I)}(\mathcal{V})$, after removal of the known value of V_{mn} at this visibility point, and where,

$$c^{(R,I)}(\mathcal{V}^{(R,I)}) = \frac{1}{2} (1 + \text{erf}(\frac{\mathcal{V}^{(R,I)}}{\sqrt{2} \sigma_{th}}))$$
 (21)

The real and imaginary parts of the visibility data are denoted by superscript (R, I) respectively.

A goodness-of-fit statistic can be computed in the form $c_{MSE}^{(R,L)} = N^{-1} \sum^{N} (\tilde{c}^{(R,I)} - c^{(R,I)})^2$, and we tabulate the geometric mean of the value for the real and imaginary parts of the data $c_{MSE} = \sqrt{c_{MSE}^R \ c_{MSE}^I}$ in table 6. This analysis demonstrates that the bootstrap resamples generated for run M3 match most closely the parent distribution, consistent with our earlier result concerning the relative performance of the model-based bootstraps used in the current study.

We note that the model-based bootstrap does require a detection of the bootstrap model in the baseline-based bootstrap model intervals Δt_b . This is broadly equivalent to the requirement that the data have sufficient SNR to allow conventional amplitude and phase self-calibration over a comparable interval. The bootstrap model is local to each interval Δt_b however, and is not equivalent to an overall model-fit to the source brightness distribution and calibration corrections for the data as a whole.

The statistical performance of the subsample bootstrap runs, S1 to S4, can be determined by examination of the goodness-of-fit statistic v_{MSE} is table 5, and the imaging estimator statistics plotted in figure 9 and figure 10. From these results it is clear that the statistical performance of this bootstrap is more sensitive to the bootstrap run parameters, here defined by the subsample delete fraction f_s , than the model-based bootstrap. Improved statistical performance is obtained for $f_s > \frac{1}{2}$ for the data used in this numerical study. This is consistent with the expected theoretical properties of the subsample bootstrap, which requires that $f_s \to 1$ as the sample size $N \to \infty$, if the bootstrap is to remain valid (Davison & Hinkley 1997).

The variance scaling factor v_f is plotted against subsample delete fraction f_s in figure 11. From theoretical considerations for the delete-d jacknife, we expect $v_f \propto (1-f_s)^{-a}$ (Davison & Hinkley 1997). For the data used in this numerical study, a relation $v_f \propto (1-f_s)^{-2}$ agrees with the data to first-order, consistent with the expected theoretical result.

Although the subsample bootstrap appears to under-perform the model-based boot-

strap, as assessed by the goodness-of-fit statistic v_{MSE} in table 5, this bootstrap has the advantage of requiring no fit to a local baseline-based bootstrap model and makes no assumption about the functional form of the long-range statistical dependence in the data. As such, it is a versatile technique which can find practical application in radio-interferometric imaging fidelity assessment.

The computing costs of the both the model-based and subsample bootstrap fidelity assessment methods are, to first order, given by the cost of the underlying calibration and imaging algorithm, scaled by the number of bootstrap resamples, N_s . We note above, however, that this algorithm is highly scalable in parallel computing environments as each resample can effectively be processed separately.

In this numerical study, we have estimated imaging fidelity by exploring only the contribution of the thermal noise variation. A recent Bayesian approach to imaging fidelity assessment for optical astronomical images is presented by Esch et al. (2004).

Bootstrap studies in general require limited statistical model assumptions and can be used directly with the measured data realization observed by a radio interferometer array. As such, they offer significant practical advantages, and we believe them to be a viable approach to imaging fidelity assessment in the automated pipeline reduction of data from current and future radio interferometers.

6. Conclusions

On the basis of this numerical study, we draw the initial conclusion that modern resampling techniques in computational statistics offer significant promise as imaging fidelity assessment techniques for common calibration and imaging processes used in radio interferometry. This conclusion applies both to the model-based bootstrap and subsample bootstrap methods. This computationally intensive approach is now tenable as a result of the recent geometric advances in available computing resources, and we believe these fidelity assessment techniques have an important role to play in automated pipeline reduction environments for modern radio telescopes.

The polarization self-calibration algorithm developed as part of this study as the framework calibration and imaging test problem, offers a new approach to interferometric polarization self-calibration which makes no assumptions regarding the form of the polarization source model.

Further work is required in assessing the statistical performance of the polarization

self-calibration algorithm and the resampling techniques over a larger set of simulated data covering a broader range of observational parameters.

This work was supported by a grant of computing time on the NCSA IA-32 Linux clusters under allocation AST 030025. We thank Drs R. Crutcher and T. Cornwell for reading the manuscript. We thank the referee for detailed comments on the manuscript which improved the paper overall.

REFERENCES

- Perley, R.A., Schwab, F.R., & Bridle, A.H., editors 1989, ASP Conf. Ser. 6, Synthesis Imaging in Radio Astronomy, A Collection of Lectures from the Third NRAO Synthesis Imaging Summer School, ed. by R.A. Perley, F.R. Schwab, & A.H. Bridle (San Francisco: ASP)
- Cawthorne, T.V., Wardle, J.F.C., Roberts, D.H., & Gabuzda, D.C. 1993, ApJ, 416, 519
- Chernick, M.R. 1999, Bootstrap Methods: A Practitioner's Guide (New York: Wiley)
- Conway, R.G., & Kronberg, P.P. 1969, MNRAS, 142, 11
- Cornwell, T.J. 1995a, AIPS++ Note 183, http://aips2.nrao.edu/docs/notes/183/183.html
- Cornwell, T.J. 1995b, AIPS++ Note 184, http://aips2.nrao.edu/docs/notes/184/184.html
- Cornwell, T.J., & Wieringa, M.H. 1996, AIPS++ Note 189, http://aips2.nrao.edu/docs/notes/189/189.html
- Cornwell, T., & Fomalont, E.B. 1999, in ASP Conf. Ser. 180, Synthesis Imaging in Radio Astronomy II, A Collection of Lectures from the Sixth NRAO/NMIMT Synthesis Imaging Summer School, ed. by G.B. Taylor, C.L. Carilli, & R. A. Perley (San Francisco:ASP), 187
- Cotton, W.D., Geldzahler, B.J., Marcaide, J.M., Shapiro, I.I., Sanroma, M., & Rius, A. 1984, ApJ, 286, 503
- Cotton, W.D. 1993, AJ, 106, 1241
- Davison, A.C., & Hinkley, D.V. 1997, Bootstrap Methods and their Applications (Cambridge: CUP)

Efron B., 1979, Annals of Statistics, 7, 1

Esch, D.N., Connors, A., Karovska, M., & van Dyk, D.A. 2004, ApJ, 610, 1213

Hamaker, J.P., Bregman, J.D., & Sault, R.J. 1996, A&AS, 117, 137

Hamaker, J.P., & Bregman, J.D. 1996, A&AS, 117, 161

Hamaker, J.P. 2000, A&AS, 143, 515

Högbom, J.A. 1974, A&AS, 15, 417

Kay, S.M. 1993, Fundamentals of Statistical Signal Processing: Estimation Theory (New Jersey: Prentice Hall)

Kellermann, K.I., & Thompson, A.R. 1985, Science, 229, 123

Kemball, A.J. 1993, Ph.D. thesis, Rhodes University

Kemball, A.J., Diamond, P.J., & Cotton, W.D. 1995, A&AS, 110, 383

Kemball, A.J., Diamond, P.J., & Pauliny-Toth, I.I.K. 1996, ApJ, 464, L55

Kemball, A.J., & Diamond, P.J. 1997, ApJ, 481, L111

Kemball, A.J. 1999, in ASP Conf. Ser. 180, Synthesis Imaging in Radio Astronomy II, A Collection of Lectures from the Sixth NRAO/NMIMT Synthesis Imaging Summer School, ed. by G.B. Taylor, C.L. Carilli, & R. A. Perley (San Francisco:ASP), 499

Kemball, A.J. 2002, in ASP Conf Ser. 206, Cosmic Masers: From Protostars to Black Holes, ed. V. Migenes & M.J. Reid (San Francisco: ASP), 359

Lahiri, S.N. 2003, Resampling Methods for Dependent Data (New York: Springer-Verlag)

Leppanen, K.J., Zensus, J.A., & Diamond, P.J. 1995, AJ, 110, 2479

Maitra, R. 1997, J. Comp. Graph. Stat., 6, 132

Morris, D., Radhakrishnan, V., & Seielstad, G.A. 1964, ApJ, 139, 551

Noordam, J.E. 1995, AIPS++ Note 182, http://aips2.nrao.edu/docs/notes/182/182.html

Noordam, J.E. 1996, AIPS++ Note 185, http://aips2.nrao.edu/docs/notes/185/185.html

Politis, D.N., Romano, J.P., & Wolf, M. 1999, Subsampling (New York: Springer-Verlag)

- Readhead, A.C.S, & Wilkinson, P.N. 1978, ApJ, 223, 25
- Roberts, D.H., Potash, R.I., Wardle, J.F.C., Rogers, A.E.E., & Burke, B.F. 1984, in IAU Symp. 110, VLBI and Compact Radio Sources, ed. R. Fanti, K. Kellermann, & G. Setti (Dordrecht:Reidel), 35
- Roberts, D.H., Brown, L.F., & Wardle, J.F.C. 1991, in ASP Conf. Ser. 19, Radio Interferometry: Theory, Techniques, and Applications, ed. by T. Cornwell & R.A. Perley (San Francisco: ASP), 281
- Roberts, D.H., Wardle, J.F.C, & Brown, L.F. 1994, ApJ, 427, 718
- Rogers, A.E.E, Hinteregger, H.F., Whitney, A.R., Counselman, C.C., Shapiro, I.I., Wittels, J.J., Klemperer, W.K., Warnock, W.W., Clark, T.A., & Hutton, L.K. 1974, ApJ, 193, 293
- Sault, R.J., Hamaker, J.P., & Bregman, J.D. 1996, A&AS, 117, 149
- Shao, J., & Tu, D. 1995, The Jackknife and Bootstrap (New York: Springer-Verlag)
- Singh, K. 1981, Annals of Statistics, 9, 1187
- Taylor, G.B., Carilli, C.L., & Perley, R.A., editors 1999, ASP Conf. Ser. 180, Synthesis Imaging in Radio Astronomy II, A Collection of Lectures from the Sixth NRAO/NMIMT Synthesis Imaging Summer School, ed. by G.B. Taylor, C.L. Carilli, & R. A. Perley (San Francisco:ASP)
- Thompson, A.R., Moran, J.M., & Swenson Jr., G.W. 2001, Interferometry and Synthesis in Radio Astronomy (2d ed.; New York: Wiley)
- Wardle, J.F.C., & Roberts, D.H. 1994, in Compact Radio Sources, ed. by J.A. Zensus & K.I. Kellermann (Green Bank: NRAO), 217
- Weiler, K.W. 1973, AA, 26, 403

This preprint was prepared with the AAS LATEX macros v5.2.

Table 1. Simulation D-term model values

VLBA antenna	$\ D^R\ $	ϕ^R (deg)	$\ D^L\ $	ϕ^L (deg)
Pie Town, NM	0.03	-57.0	0.01	23.0
Kitt Peak, AZ	0.02	40.0	0.01	-5.0
Los Alamos, NM	0.03	10.0	0.05	13.0
Brewster, WA	0.04	87.0	0.02	3.0
Fort Davis, TX	0.09	-15.0	0.03	56.0
St. Croix, VI	0.01	-52.0	0.01	29.0
North Liberty, IA	0.05	77.0	0.01	-23.0
Owens Valley, CA	0.03	47.0	0.01	43.0
Mauna Kea, HI	0.03	-7.0	0.06	83.0
Hancock, NM	0.03	-27.0	0.02	35.0

Note. — The D-terms tabulated here in a circular basis translate to a D Jones matrix for antenna m of the form:

$$D_{m} = \begin{pmatrix} 1 & \|D^{R}\| e^{j\phi^{R}} \\ \|D^{L}\| e^{j\phi^{L}} & 1 \end{pmatrix}$$
 (22)

Table 2. Simulation source model parameters

	$\triangle \alpha$ (mas)	$\triangle \delta$ (mas)	b_{maj} (mas)						<i>V</i> (Jy)
1	0		0.2			1		0.1	0
2	-0.5	+0.1	0.3	0.1	-10	1	0	0.25	-0

Table 3. Model-based bootstrap run parameters

Run code	$\max(N_p)$	$\triangle t_b \; (\mathrm{sec})$
M1	1	60
M2	1	150
M3	1	300
M4	2	900

Note. — $\max(N_p)$ is the maximum degree of the model polynomial used in each bootstrap model interval Δt_b .

Table 4. Subsample bootstrap run parameters

Run code	f_s
S1	0.125
S2	0.25
S3	0.5
S4	0.75

Note. — f_s is the fraction of data deleted in each subsample realization

Table 5. Bootstrap performance statistics

Code	v_f	$v_{MSE} \times 10^{-10})$
M1	1.00	2.95
M2	1.01	2.28
M3	1.00	2.19
M4	1.02	2.36
S1	0.157	6.43
S2	0.319	5.15
S3	0.782	3.42
S4	2.03	3.04

Note. — The bootstrap performance measures, v_f and v_{MSE} , are defined in the main text.

Table 6. MSE of CDF fit to parent distribution

Code	$c_{MSE} \times 10^{-4})$
M1 M2	11.1 25.5
M3	5.35
M4	8.07

Note. — The MSE of the CDF fit to the parent distribution, c_{MSE} , is defined in the main text. The value tabulated here is for visibility row 1000 in cross-correlation LR. For reference, the corresponding value from the Monte Carlo sample is 3.48×10^{-4} .

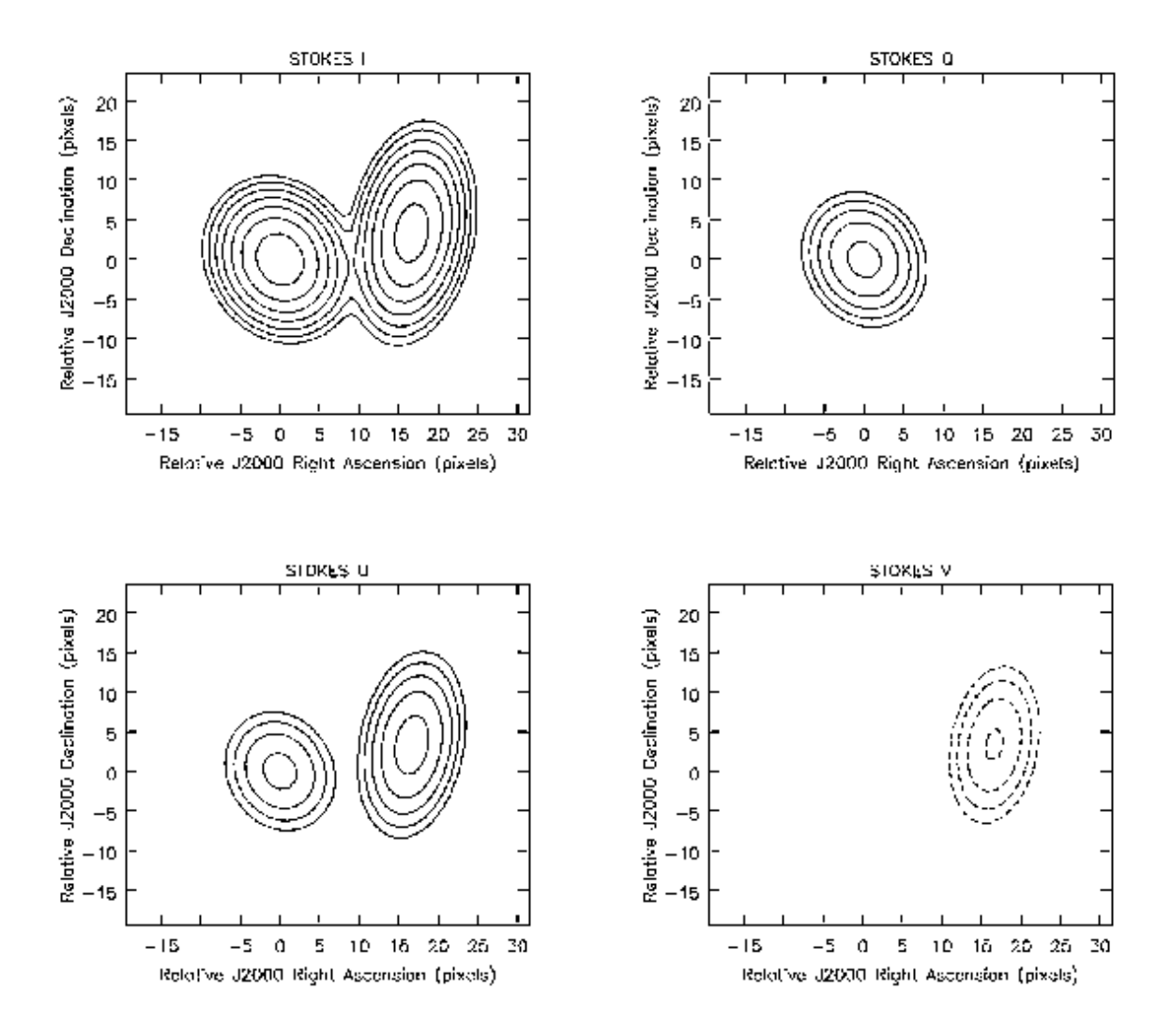


Fig. 1.— Simulation source model, convolved with a circular restoring beam of 156.007 μas , plotted in Stokes $\{I,Q,U,V\}$, using contour levels of $\{-64,\ -32,\ -16,\ -8,\ -4,\ -2,\ -1,\ 1,\ 2,\ 4,\ 8,\ 16,\ 32,\ 64\}\times 4.434\times 10^{-3}$ Jy per beam. The peak brightness in Stokes $\{I,Q,U,V\}$ is $4.434\times 10^{-1},\ 8.867\times 10^{-2},\ 9.591\times 10^{-2},\ and <math>-3.836\times 10^{-2}$ Jy per beam respectively.

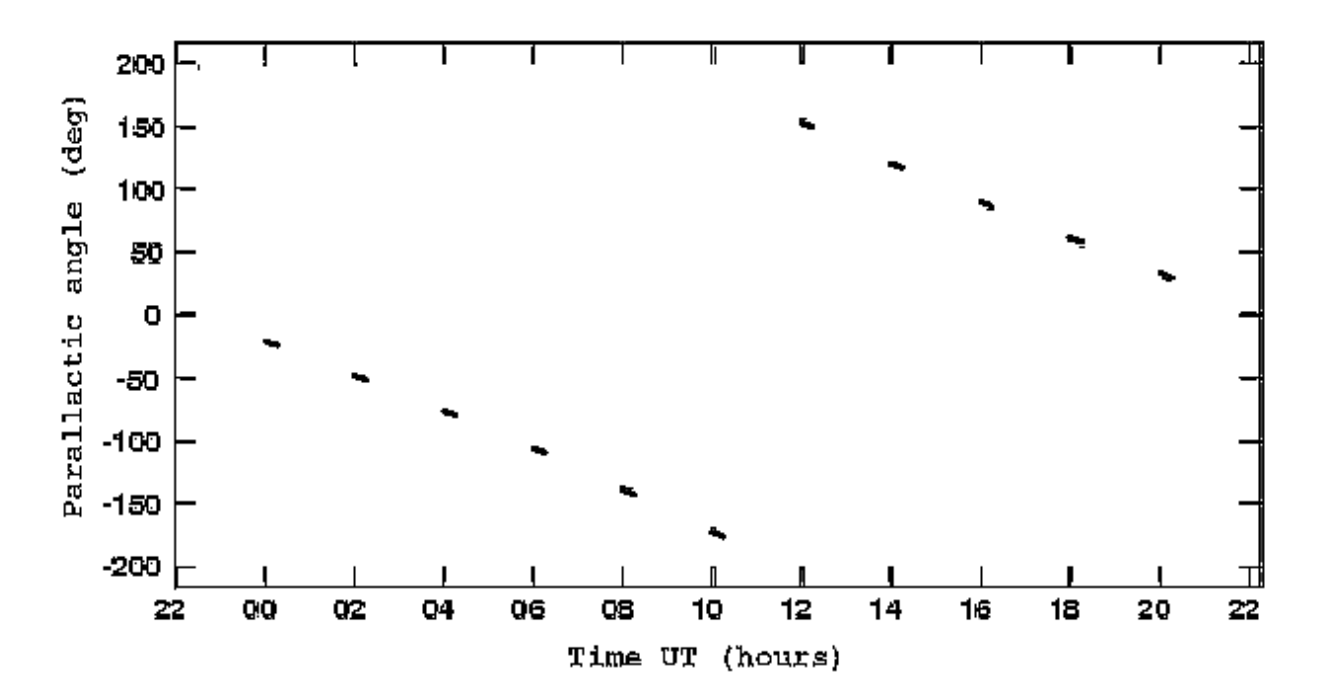


Fig. 2.— Parallactic angle variation at the Pie Town antenna for the data used in the Monte Carlo simulations.

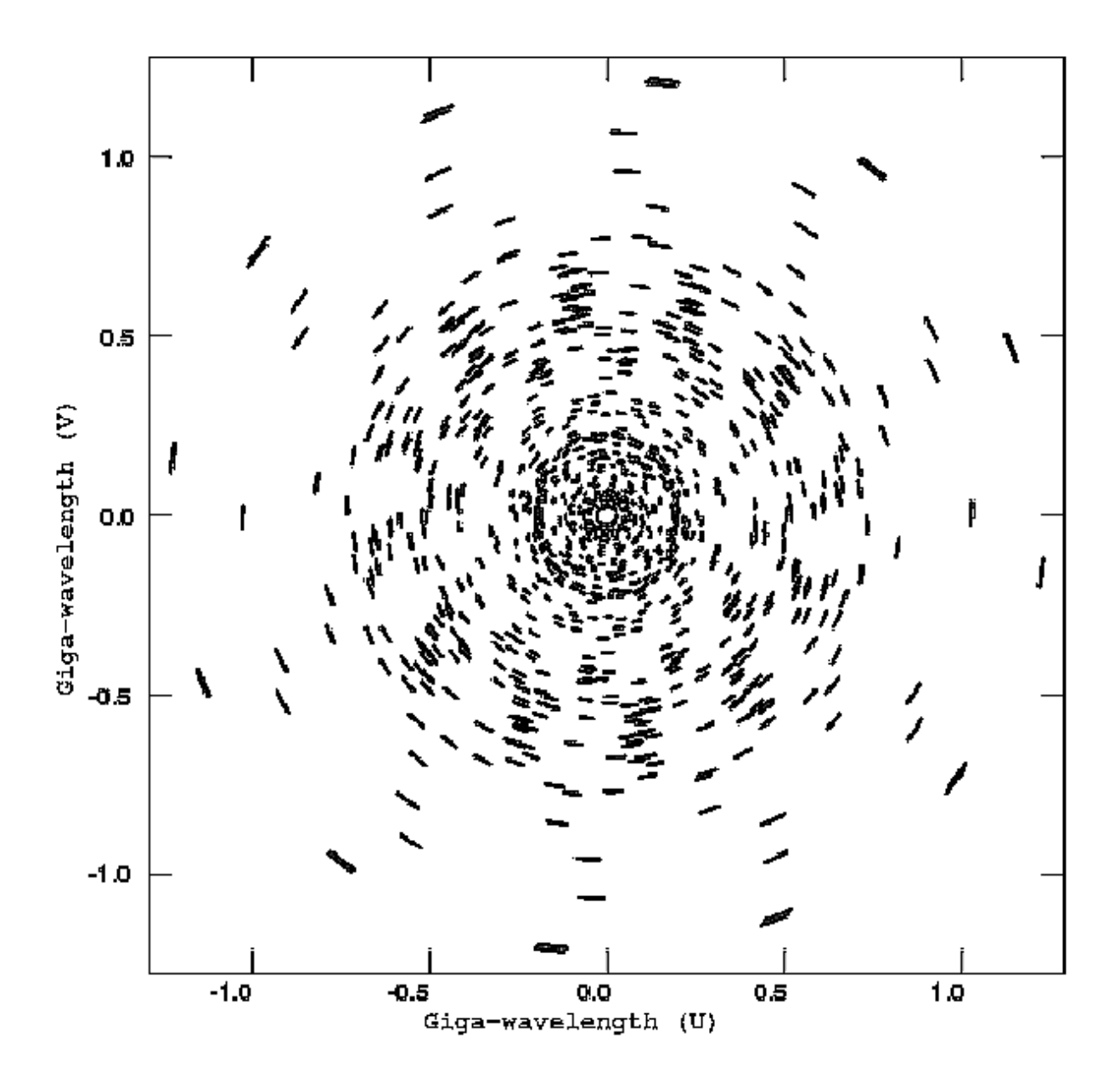


Fig. 3.— uv-coverage for the data used in the Monte Carlo simulations. The simulated source has coordinates ($\alpha_{2000}=12^h,\ \delta_{2000}=+80^{\rm deg}$)

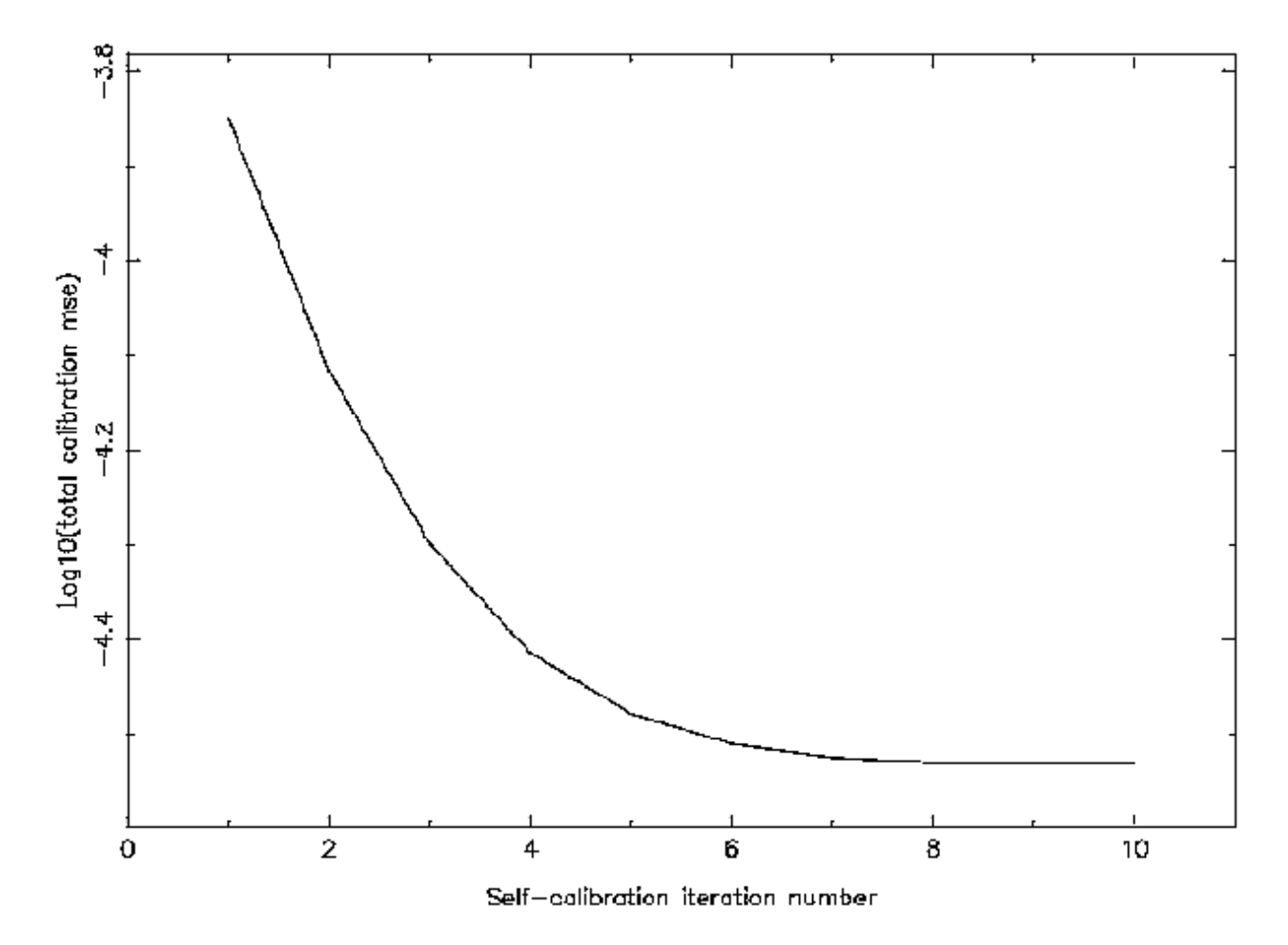


Fig. 4.— Mean-squared error in the off-diagonal D Jones matrix elements, solved for using polarization self-calibration, averaged over all antennas in the Monte Carlo simulation, and plotted on a logarithmic scale against self-calibration iteration number. The total calibration MSE is computed as: $\frac{1}{2N} \sum_{p \in (R,L)} \sum_{m}^{N} (d_m^p - \check{d}_m^p) (d_m^p - \check{d}_m^p)^*, \text{ where } d_m^p \text{ is the instrumental polarization determined by the solver, and } \check{d}_m^p \text{ is the true value used to generate the simulated data. The instrumental polarization terms are defined in equation 7.$

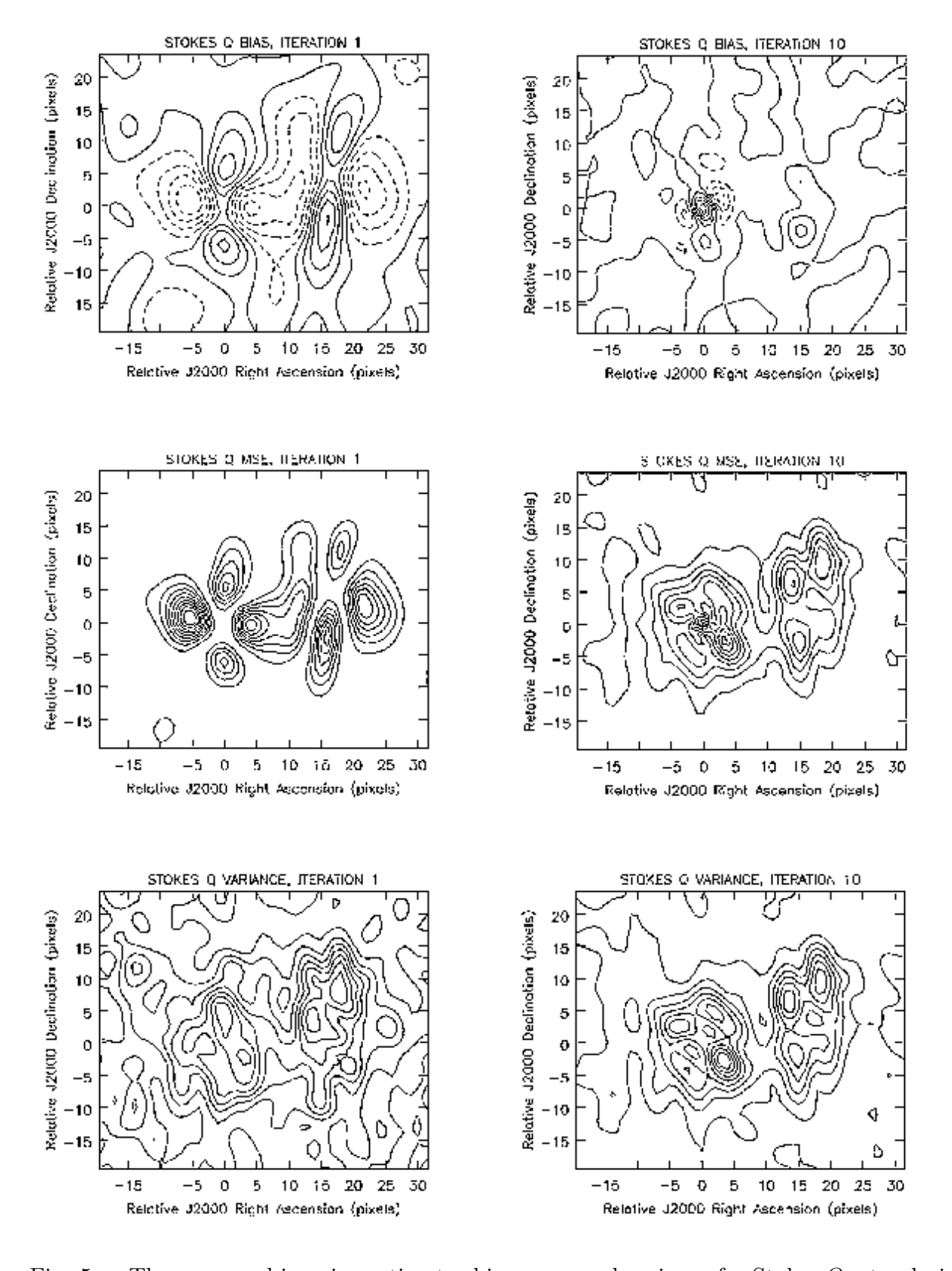


Fig. 5.— The measured imaging estimator bias, mse, and variance for Stokes Q, at polarization self-calibration iteration numbers 1 and 10, for the Monte Carlo sample. Contour levels for the bias plots are at levels of $\{0.2n, n = -5, 5\}$ of the local absolute maximum value $(4.566 \times 10^{-3} \text{ at iteration 1, and } 1.009 \times 10^{-3} \text{ at iteration 10})$. Contour levels for the mse and variance plots are at $\{0.1n, n = 1.10\}$ of the local maximum. The peak mse is 2.155×10^{-5}

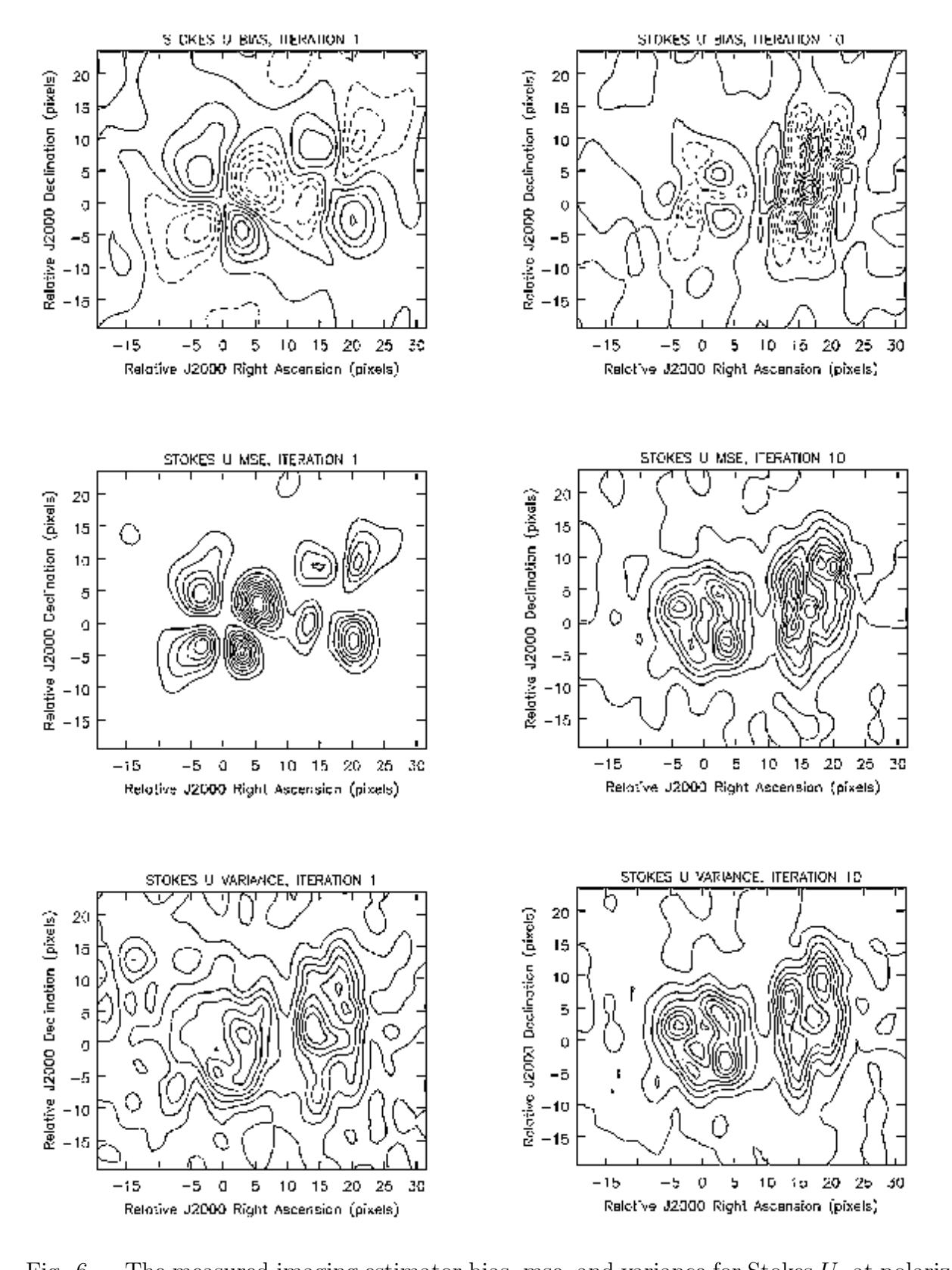


Fig. 6.— The measured imaging estimator bias, mse, and variance for Stokes U, at polarization self-calibration iteration numbers 1 and 10, for the Monte Carlo sample. Contour levels for the bias plots are at levels of $\{0.2n, n = -5, 5\}$ of the local absolute maximum value $(4.476 \times 10^{-3} \text{ at iteration 1, and } 8.261 \times 10^{-4} \text{ at iteration 10})$. Contour levels for the mse and variance plots are at $\{0.1n, n = 1, 10\}$ of the local maximum. The peak mse is 2.082×10^{-5}

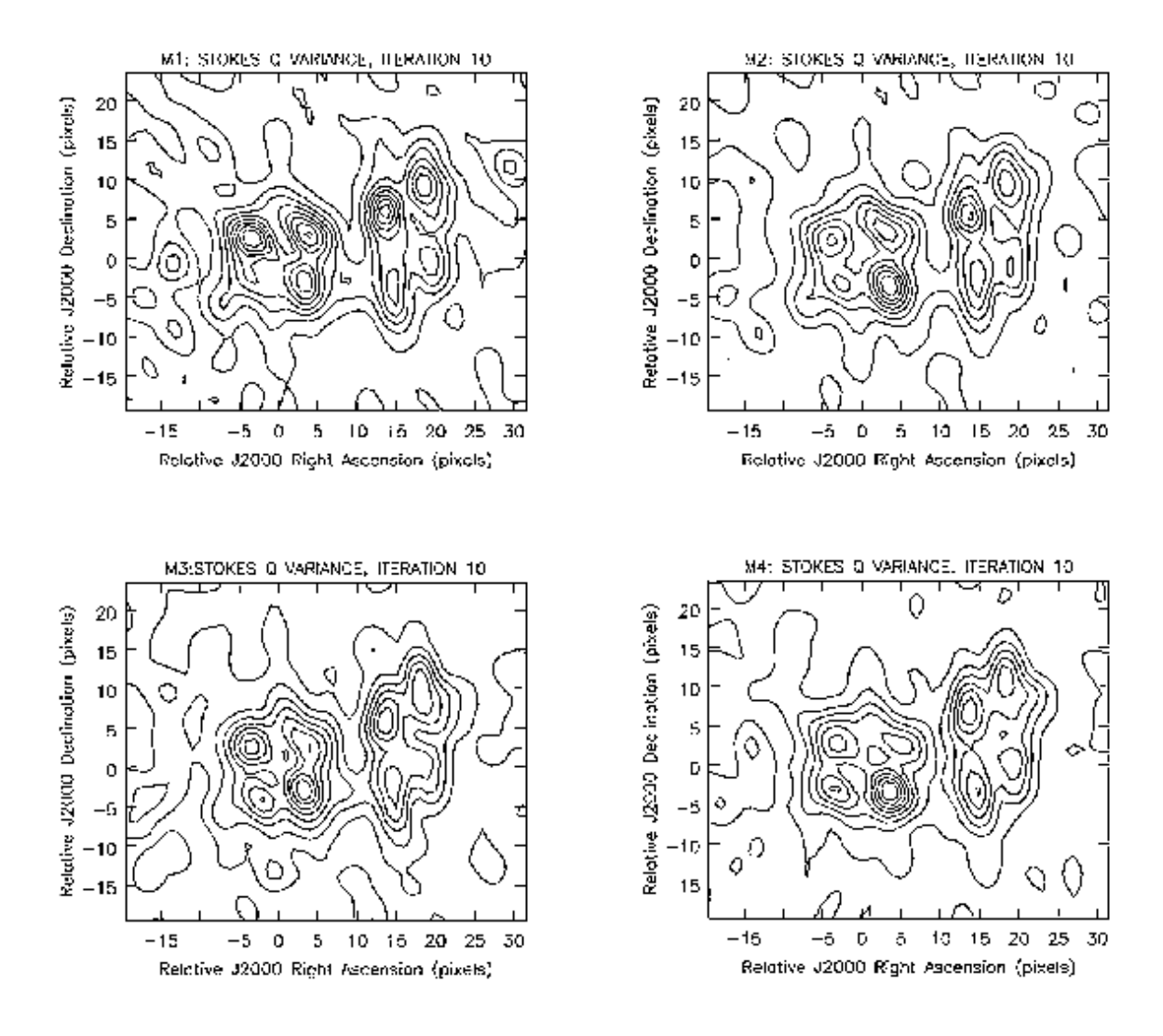


Fig. 7.— The measured imaging estimator Stokes Q variance for the model-based bootstrap runs M1-M4, at the final polarization self-calibration iteration number 10. The contour levels are plotted at $\{0.1n, n = 1, 10\}$ of the local maximum value, which are 1.666×10^{-6} (M1), 1.852×10^{-6} (M2), 1.758×10^{-6} (M3), and 1.855×10^{-6} (M4) (Jy per beam)². The parameters for the bootstrap run codes M1-M4 are defined in table 3.

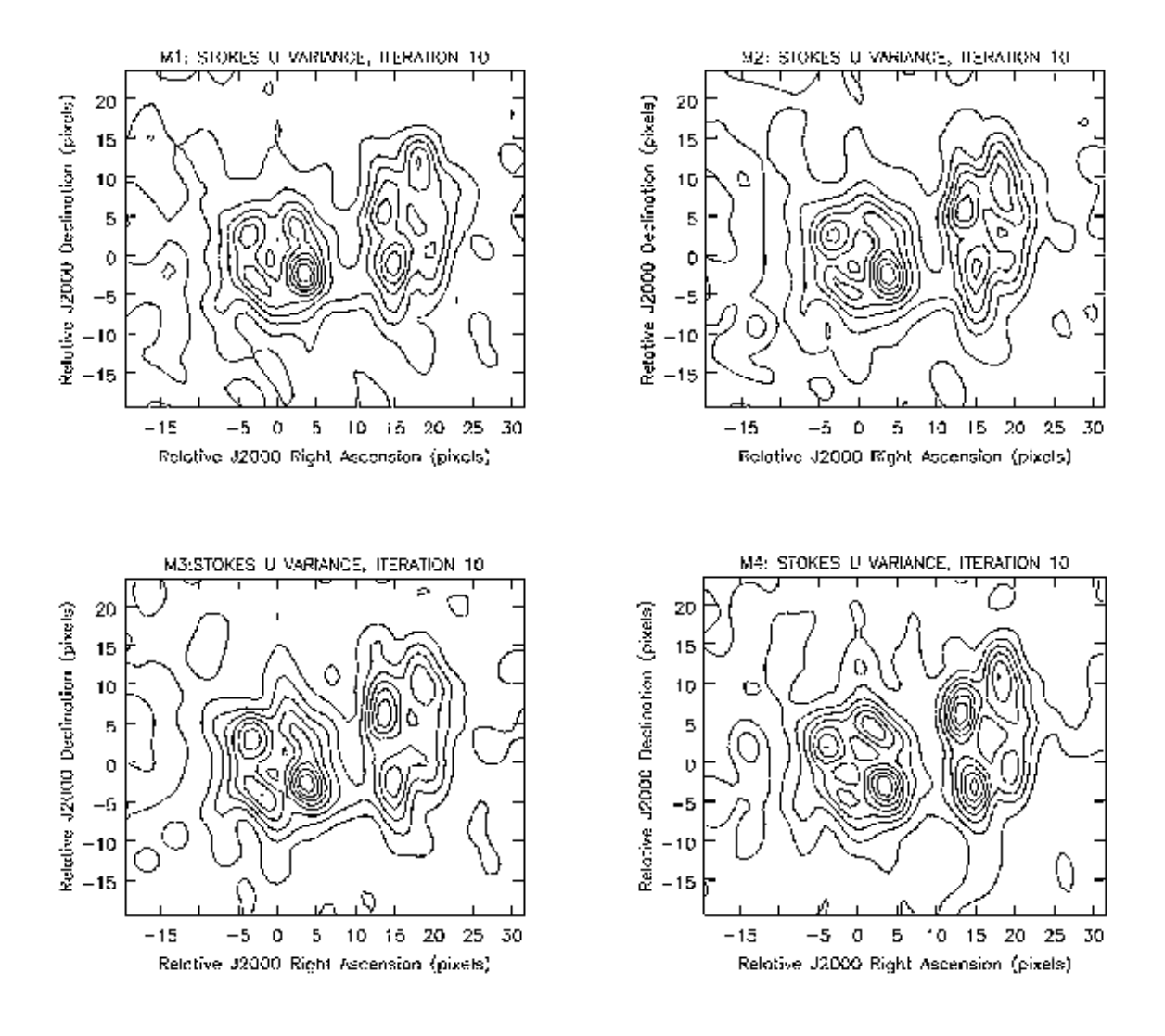


Fig. 8.— The measured imaging estimator Stokes U variance for the model-based bootstrap runs M1-M4, at the final polarization self-calibration iteration number 10. The contour levels are plotted at $\{0.1n, n = 1, 10\}$ of the local maximum value, which are 1.737×10^{-6} (M1), 1.765×10^{-6} (M2), 1.843×10^{-6} (M3), and 1.889×10^{-6} (M4) (Jy per beam)². The parameters for the bootstrap run codes M1-M4 are defined in table 3.

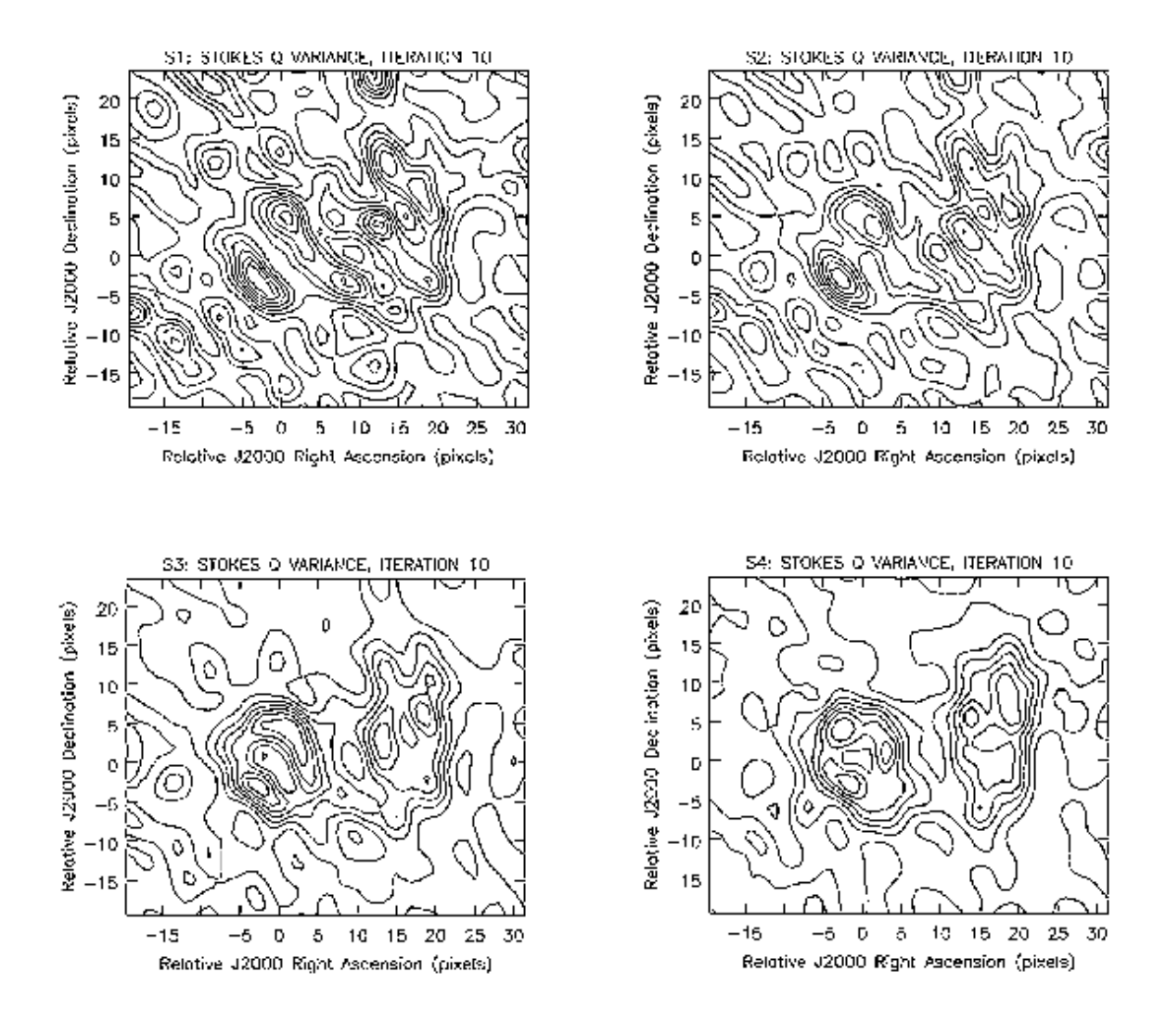


Fig. 9.— The measured imaging estimator Stokes Q variance for the subsample bootstrap runs S1-S4, at the final polarization self-calibration iteration number 10. The contour levels are plotted at $\{0.1n, n = 1, 10\}$ of the local maximum value, which are 1.827×10^{-7} (S1), 3.849×10^{-7} (S2), 7.994×10^{-7} (S3), and 1.890×10^{-6} (S4) (Jy per beam)². The parameters for the bootstrap run codes S1-S4 are defined in table 4.

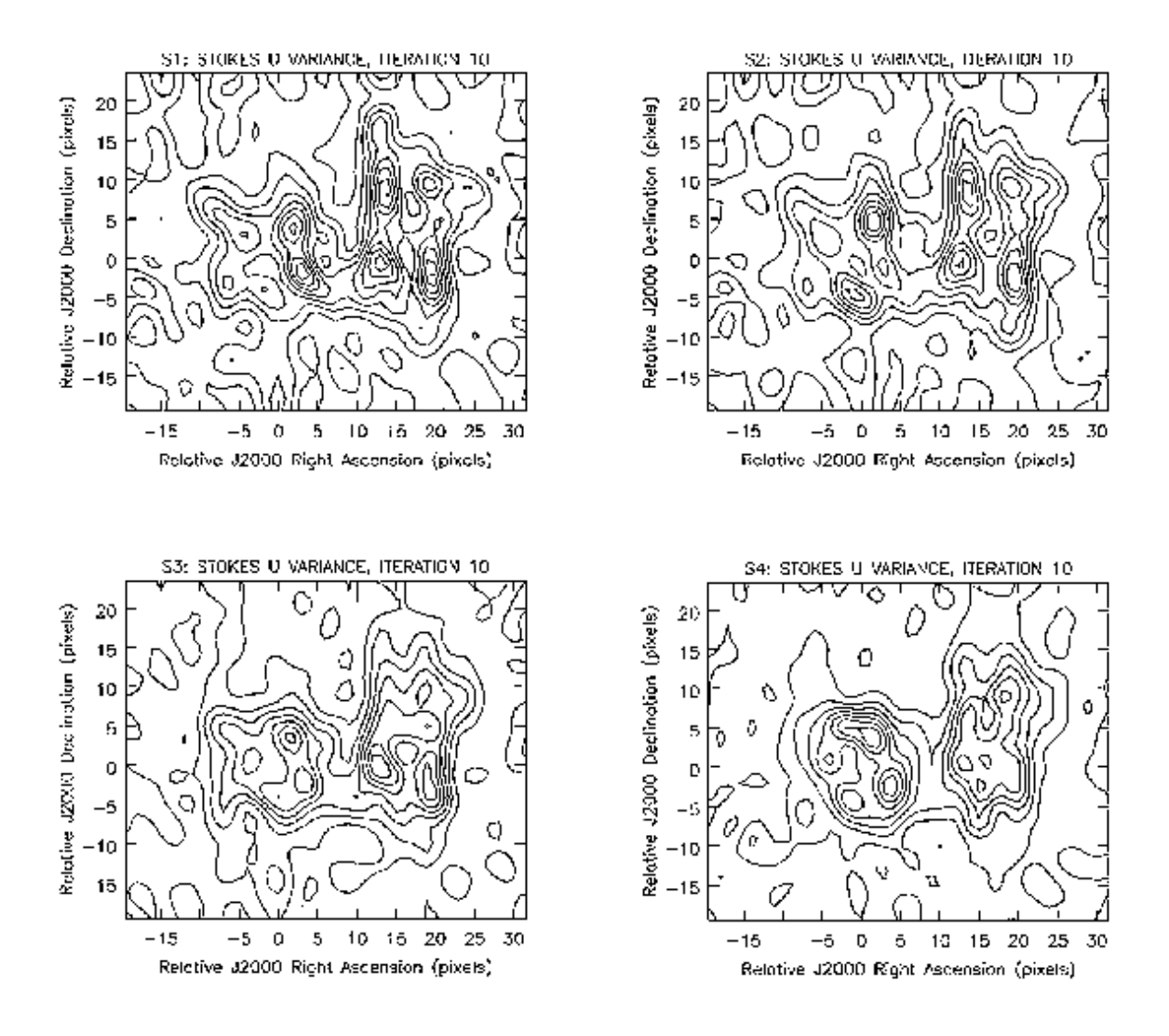


Fig. 10.— The measured imaging estimator Stokes U variance for the subsample bootstrap runs S1-S4, at the final polarization self-calibration iteration number 10. The contour levels are plotted at $\{0.1n, n = 1, 10\}$ of the local maximum value, which are 1.817×10^{-7} (S1), 3.737×10^{-7} (S2), 8.262×10^{-7} (S3), and 2.100×10^{-6} (S4) (Jy per beam)². The parameters for the bootstrap run codes S1-S4 are defined in table 4.

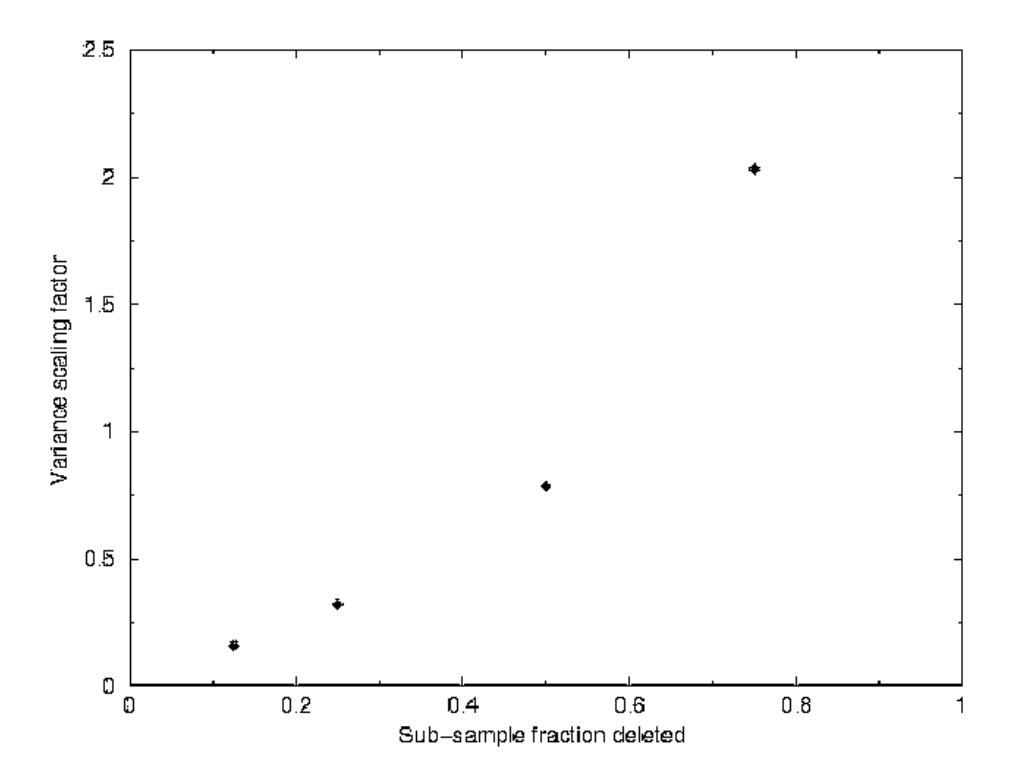


Fig. 11.— The variance scaling factor, v_f , plotted against the subsampling delete fraction, f_s .

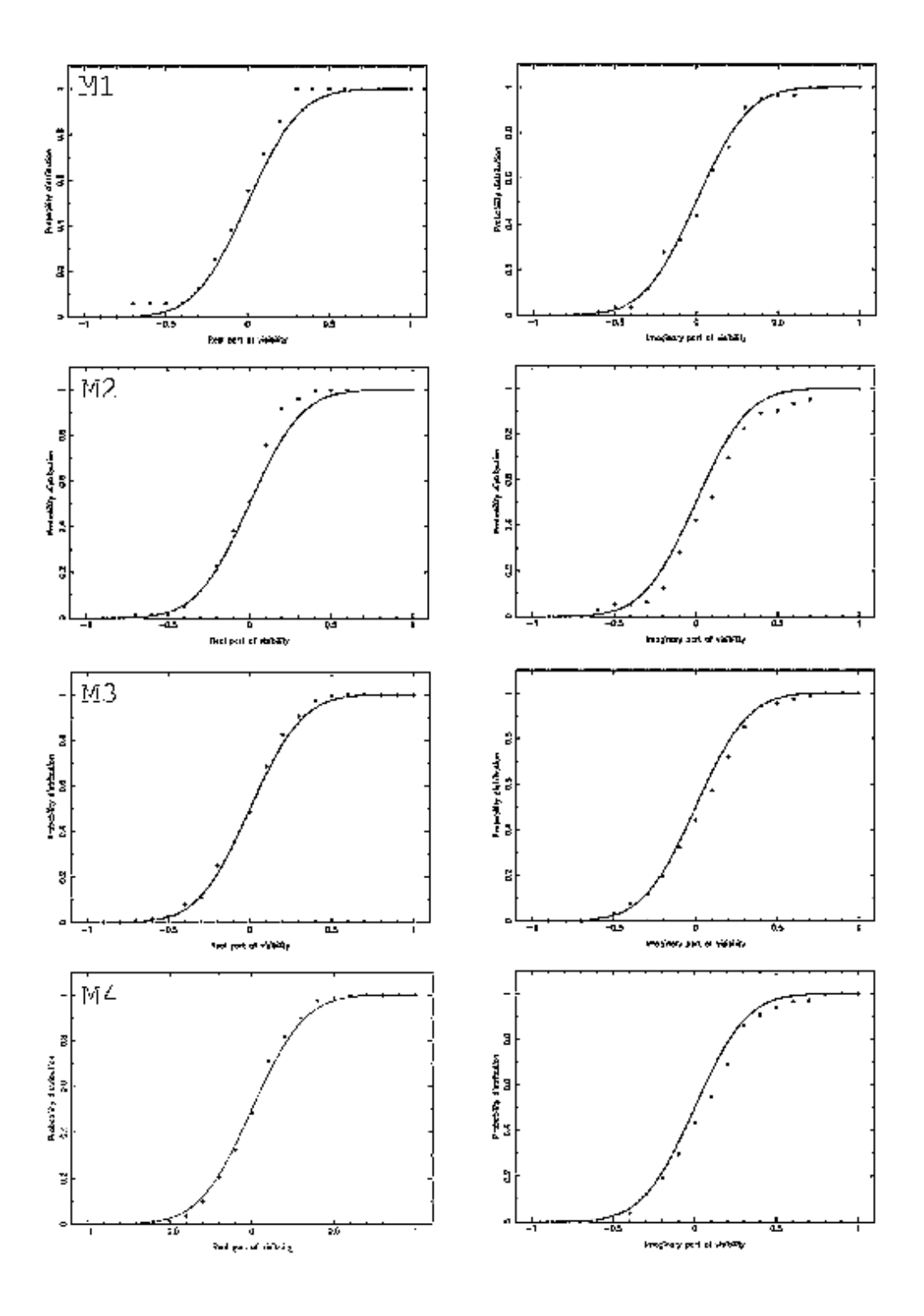


Fig. 12.— The empirical CDF for visibility row 1000, polarization cross-correlation LR, for the model-based bootstrap resamples M1 to M4. The CDF for the real part of the visibility data is plotted in the left column, and the CDF for the imaginary part of the visibility data in right column. The solid line is the expected normal CDF from the parent distribution. All data have been centered by subtracting the expected visibility value V_{mn} at this visibility

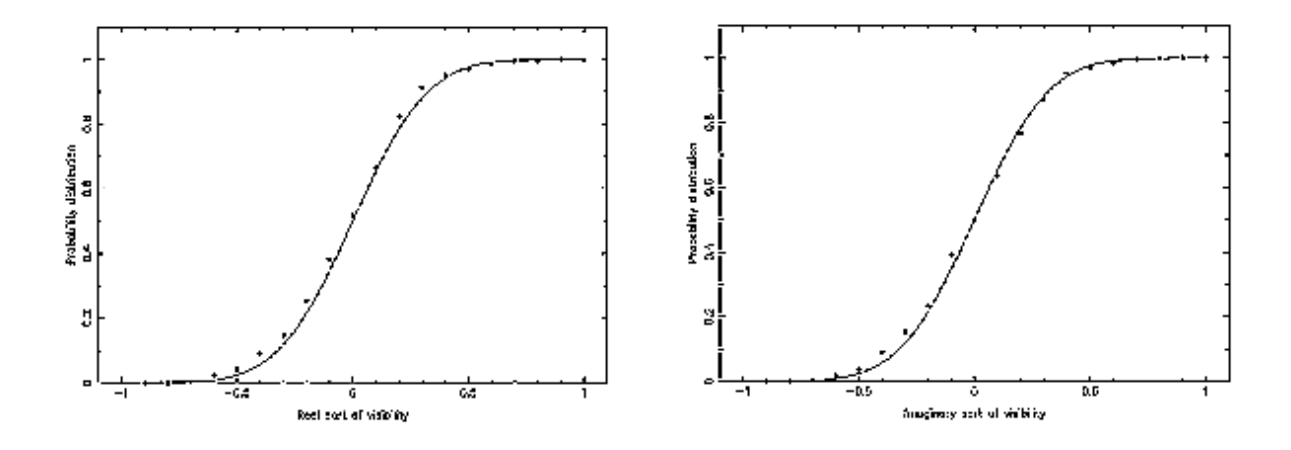


Fig. 13.— The empirical CDF for visibility row 1000, polarization cross-correlation LR, for the Monte Carlo sample. The CDF for the real part of the visibility data is plotted in the left column, and the CDF for the imaginary part of the visibility data in the right column. The solid line is the expected normal CDF from the parent distribution. All data have been centered by subtracting the expected visibility value V_{mn} at this visibility row number.